RSC Advances

ROYAL SOCIETY OF CHEMISTRY

www.rsc.org/advances

Structure-Composition Relationships of Bioactive Borophosphosilicate Glasses Probed by Multinuclear ^{11}B, ^{29}Si, and ^{31}P Solid State NMR

Yang Yu and Mattias Edén*

Physical Chemistry Division, Department of Materials and Environmental Chemistry, Stockholm University, SE-106 91 Stockholm, Sweden

*Corresponding author. E-mail: *mattias.eden@mmk.su.se*

Keywords: borosilicate glass, glass structure, B and P speciations, network polymerization, 45S5 Bioglass

Abstract

By combining ^{11}B, ^{29}Si, and ^{31}P nuclear magnetic resonance (NMR) experimental results, we present a comprehensive structural investigation of 15 borophosphosilicate (BPS) glasses of the Na_2O–CaO–B_2O_3–SiO_2–P_2O_5 system: in two base compositions comprising 46 mol% ("S46") and 49 mol% ("S49") SiO_2, progressive replacements of SiO_2 by B_2O_3 were performed at a constant total Na_2O and CaO content. The S46 glass members constitute B-bearing analogs of "45S5 Bioglass" that is utilized extensively for bone grafting in periodontal and orthopedic surgery. Orthophosphate ions prevail throughout all structures, while the silicate network polymerization increases slightly for growing amount of B_2O_3 in the glass. ^{11}B NMR revealed continuous $BO_3 \rightarrow BO_4$ conversions

for increasing B_2O_3 content, with asymptotic fractions of 34% and 43% of $B^{[4]}$ coordinations out of the borate speciation observed for the series of S46 and S49 glasses, respectively. While all BPS glasses are homogeneous across a μm-scale, strong preferences for $B^{[3]}$–O–$B^{[3]}$ and $B^{[4]}$–O–$Si^{[4]}$ bond formation lead to structures comprising (sub)nm-sized domains of BO_3 groups in boroxol rings and borosilicate networks built by SiO_4 and BO_4 tetrahedra. These borate/borosilicate networks are merged mainly by $B^{[4]}$(3Si) and $B^{[3]}$(1Si) moieties in Si-rich BPS glasses (where each value in parentheses specifies the number of bonds to Si atoms), while $B^{[4]}$(3Si) and $B^{[4]}$(2Si) groups are the dominant network contact points in the B-rich glasses. We discuss the partitioning of non-bridging oxygen ions between the BO_3 and SiO_4 groups, the relative propensities for $B^{[4]}$–O–$Si^{[4]}$ and $B^{[4]}$–O–$B^{[3]}$ bond formation, as well as the expected bearings of our proposed BPS structural model for the glass degradation in aqueous media, where we identify the fractional population of $B^{[4]}$ coordinations and the silicate network connectivity to constitute the dissolution-controlling parameters.

1 Introduction

The elements Al, B, P, and Si build the networks of a vast majority of all oxide-based glasses.[1–3] Most of them involve one or two network-forming species, while the development and structural characterization of glasses incorporating three (or more) network formers are much less explored. Yet, they are of interest for the fundamental understanding of glass Chemistry, where an improved insight into such mixed-former glass networks will assist the tailoring of their physical, chemical, and mechanical glass properties.

Our study concerns *borophosphosilicate* (BPS) glasses that show great promise for bone-grafting applications.[4–14] On their contact with body fluids, such *bioactive glasses* (BGs)[9,15–17] integrate with the bone/tooth by forming a surface layer of hydroxy-carbonate apatite (HCA), whose com-

position closely mimics bone mineral. Some of the alkali/alkaline-earth-rich borate and borosilicate glasses involved B for Si substitutions of already existing phosphosilicate BGs,[4–6,11–13] such as the "19-93"[18] and the "45S5 Bioglass®"[15,17] compositions; the latter is soda-lime-silica based with molar equivalents 24.6Na_2O–26.7CaO–46.1SiO_2–2.6P_2O_5 and has been in clinical use for decades.[17] Phosphosilicate BGs feature rings and chains of interconnected silicate tetrahedra (SiO_4).[3,17] The incorporation of BO_3/BO_4 borate groups modifies the glass network by the formation of Si–O–B and B–O–B bonds. Compared with phosphosilicate BGs, the borate-based counterparts degrade faster in aqueous media[19,20] and are claimed to convert more completely into HCA.[4–9,14] The glass degradation is tunable by varying the n_B/n_{Si} molar ratio.[4,5] Moreover, the dissolution products of B-bearing BGs may promote bone growth and angiogenesis,[9,13] as well as stimulating RNA synthesis in fibroblast cells[21] to further aid the bone regeneration.

The present report targets two series of Na_2O–CaO–B_2O_3–SiO_2–P_2O_5 glasses (one based on the "45S5" composition[15]), where SiO_2 is replaced by B_2O_3 at a *fixed total* Na_2O and CaO content. These network modifier-rich (boro)phosphosilicate glasses exhibit fragmented glass networks, mainly built by ring/chain motifs of interlinked SiO_4, BO_4, and BO_3 polyhedra. The local glass structures were probed by a combination of magic-angle spinning (MAS) ^{11}B, ^{29}Si, and ^{31}P NMR experiments. Besides providing the first comprehensive structural account on B-substituted BGs (such as the 45S5 based glasses[4,6,13]), we demonstrate that P-richer bioactive BPS glasses are feasible to prepare: increasing the P content of a silicate-based BG is believed to promote its HCA formation *in vitro*[17,22,23] and P-rich BPS glass analogs should consequently also be beneficial.

This work also complements the few existing structural reports on BPS glasses that generally targeted the compositional space of low modifier contents relative to P and Si,[24–26] encompassing M_2O–B_2O_3–SiO_2–P_2O_5 glasses of low P and alkali metal M={Na, K} contents[24,26] or P-rich compositions of the Na_2O–(CaO)–B_2O_3–SiO_2–P_2O_5 system.[25,27] For the latter, P assumes its

usual role as a network former in the guise of phosphate chains that are cross-linked to the silicate/borate networks.[24,25] This structural scenario is also shared by P-rich $M_{(2)}O$–SiO_2–P_2O_5 glasses,[28,29] but contrasts markedly with that for the fragmented networks of *bioactive* phosphosilicate glasses, where P is typically a minor component ($\lesssim 6$ mol% P_2O_5) and predominantly forms *ortho*phosphate (PO_4^{3-}) anions[22,23,30–34] that are charge-balanced by Na^+/Ca^{2+} and distributed randomly at interstitial positions around the silicate network.[32,35] This property ensures a rapid release of phosphate moieties when the BG is subjected to (simulated) body fluids.[23,33,36] One of the goals of the present work is the verification that this favorable structural role of P remains when substantial amounts of borate groups are incorporated into the glass structure. Previous work on Na_2O–B_2O_3–SiO_2–P_2O_5 glasses[26] suggests this not to apply for compositions featuring (significantly) lower Na contents than the total modifier (Na^+, Ca^{2+}) reservoirs of the present glasses.

2 Structural Features of Borophosphosilicate Glasses

2.1 Basic Building Blocks

The present soda-lime BPS glasses involve three traditional glass network-forming species: B, P, and Si. Regarding the structural role of P, earlier reports from Na–B–Si–P–O glasses of relatively low amounts of Na but with comparable Si and P contents as our current glasses revealed a dominance of $P_2O_7^{4-}$ diphosphate groups and P–O–B structural fragments,[24,26] suggesting a traditional network-forming role of P. However, as demonstrated in section **4.1**, very few phosphate tetrahedra in the present *modifier-rich* BPS structures bind to network-forming groups and the P speciation is dominated by *ortho*phosphate anions, denoted Q_P^0. Henceforth, Q_P^n (Q_{Si}^n) labels a PO_4 (SiO_4) tetrahedron with n *bridging oxygen* (BO) species[1–3] that share corners with neighboring tetrahedra. The remaining $4-n$ tetrahedral corners represent *non-bridging* oxygen (NBO) ions that are charge-

balanced by electropositive metal ions (herein, Na^+ and Ca^{2+}).

In contrast with the structure of P-rich (boro)phosphosilicate glasses that also feature SiO_5/SiO_6 polyhedra,[25,28,29] Si is exclusively present in tetrahedral coordination ($Si^{[4]}$) in modifier-rich/P-poor BPS glasses (see section **4.2**),[24–26] where it assumes a set of interconnected $\{Q^n_{Si}\}$ groups. Si may also bond to the two B coordinations, $B^{[3]}$ and $B^{[4]}$, which represent trigonal BO_3 and tetrahedral $[BO_4]^-$ moieties, respectively.[3,37–39] Here $B^{[p]}(m\text{Si})$ labels a $B^{[p]}$ species with m B–O–**Si** bonds.

The Na^+/Ca^{2+} cations play a dual structural role, where they partially balance the negatively charged $[BO_4]^-$ and $\{Q^0_P, Q^1_P\}$ moieties, whereas the remaining cations are termed *network modifiers* because they reduce the glass network polymerization by breaking $Si/B^{[3]}$–O–$Si/B^{[3]}$ bonds, thereby driving BO→NBO conversions.[1–3] The polymerization degree associated with a network-forming species E may be described by its *average* number of BO atoms per polyhedron ($\overline{N}^E_{BO}$),[3,23,33,40] which is often referred to as the *network connectivity*.[22,41,42] For silicate-based glasses, the *silicate* network connectivity ($\overline{N}^{Si}_{BO}$) may be derived from the set $\{x^n_{Si}\}$ accessible by ^{29}Si NMR.[1–3] Herein, the symbol "x" is reserved for *fractions*, where x^n_E labels the fractional population of Q^n_E out of the entire $\{Q^n_E\}$ speciation ($0 \leqslant n \leqslant 4$).

Concerning the B partitioning among $B^{[3]}/B^{[4]}$ coordinations and their precise structural relationship relative to the silicate tetrahedra, no clear consensus is reached for BPS glasses[24–27] and the compositional space relevant for *bioactive* glasses remains essentially unexplored. Yet, these aspects have been intensively investigated for the limiting borosilicate systems,[2,3,6,37,39,43–54] notably so for Na_2O–B_2O_3–SiO_2 glasses. For the latter stoichiometric compositions parametrized as $R\text{Na}_2\text{O}$–B_2O_3–$K\text{SiO}_2$, Bray and co-workers[37,38] proposed a structural model that provides the relative $\{B^{[4]}, B^{[3]}\}$ populations for variable molar ratios K and R; it is henceforth referred to as the Yun-Dell-Bray-Xiao (YDBX) model. It predicts that for low Na_2O contents (*i.e.*, small R-values), $B^{[3]} \rightarrow B^{[4]}$ conversions occur up to $R \leqslant R_{max} = K/16 + 1/2$,[38] meaning that Na^+ solely acts to

charge-balance the $[BO_4]^-$ tetrahedra. Consequently, for all compositions with $R < R_{max}$, the borosilicate structure only comprises $B^{[3]}$–O–$B^{[3]}$, Si–O–Si, and $B^{[4]}$–O–Si bonds, the latter forming $B^{[4]}(OSi)_4$ groups. NBO species only exist when $R > R_{max}$, where they initially enter solely at the SiO_4 tetrahedra, whereas the BO_3 groups starts accommodating NBO ions for Na-richer compositions with $R > (K + 1)/4$.[38]

The YDBX structural picture provides reasonable predictions of the B speciation in Na–B–Si–O glasses, and sometimes also for some other M^+/M^{2+} cation-bearing amorphous borosilicates. However, the model was formulated solely with insight from ^{11}B NMR, and subsequent studies indicate its limitations: overall, the borosilicate glass structure is less ordered than suggested by the YDBX model and the NBO ions are more evenly distributed among SiO_4 and BO_3 groups[45,46,48–53] compared with the YDBX scenario. Moreover, the {BO_3, BO_4, SiO_4} network building blocks are markedly more intermixed, with all types of $B^{[3]}/B^{[4]}$–O–$B^{[3]}/Si$ linkages encountered,[39,46–54] albeit the preferences of B–O–Si bond formation decreases in the order $B^{[4]}$>$B^{[3]}$(non-ring)>$B^{[3]}$(ring).[50–52] Here "ring" specifies BO_3 groups that exclusively form *boroxol* (B_3O_6) rings, as present in vitreous B_2O_3 and borate glasses,[2,3,39,55] whereas "non-ring" implies linkages to BO_4/SiO_4 tetrahedra.[50–54,56] To avoid local negative charge accumulation, $[BO_4]^-$ tetrahedra involve solely BO (as opposed to NBO) species,[3,37,38,40,53] while $B^{[4]}$–O–$B^{[4]}$ bridges are strongly disfavored, or even absent.[1–3,37,38,50–53] Herein, we explore the composition-dependence of the B speciation in the more complex soda-lime BPS glass system, targeting NBO-richer networks than those thoroughly investigated in the ternary/quaternary $M_{(2)}O$–($M'O$)–B_2O_3–SiO_2 systems.

2.2 Our Borophosphosilicate Glass Design

Table **1** lists our targeted Na_2O–CaO–B_2O_3–SiO_2–P_2O_5 glass compositions. Each is labeled S$N_p(q)$, where N is the *sum* of SiO_2 and B_2O_3 contents in mol%, while p and q represent the mol% of P_2O_5

and B_2O_3, respectively. Note that $S46_{2.6}(0)$ corresponds to the widely utilized "45S5 Bioglass" composition.[15,17] When collectively referring to all its members, we employ the nomenclature "S46" and "S49" for the two series, which mainly differ in (*i*) the Si contents of the two base compositions, $S46_{2.6}(0)$ and $S49_{4.0}(0)$, and thereby their glass-network polymerization degrees reflected in the corresponding silicate network connectivities[22,23,33] $\overline{N}^{\mathrm{Si}}_{\mathrm{BO}}$=2.11 and $\overline{N}^{\mathrm{Si}}_{\mathrm{BO}}$=2.54; (*ii*) the P_2O_5 contents that are constant at 2.6 mol% and 4.0 mol% *within* each respective set; (*iii*) the relative Na/Ca amounts, with the molar ratios $n_{\mathrm{Na}}/n_{\mathrm{Ca}} = x_{\mathrm{Na}}/x_{\mathrm{Ca}}$ being 1.84 and 2.08, respectively, while the *sum* $x(\mathrm{Na_2O}) + x(\mathrm{CaO})$ remains constant within each S46 and S49 family, where x_E or $x(E)$ denotes the molar fraction of species E.

The precise glass forming region of the complex Na_2O–CaO–B_2O_3–SiO_2–P_2O_5 system is unknown and is currently being explored by us. Preliminary results indicate that the S49 series may allow higher B_2O_3 substitution levels than the $S49_{4.0}(24)$ glass included in the present NMR study. However, it remains unclear how much further the amount of P may be increased for BPS glasses with significant B contents.

As demonstrated in section **4.1**, the phosphate speciation in our Na_2O–CaO–B_2O_3–SiO_2–P_2O_5 glasses is dominated by *ortho*phosphate (Q^0_{P}) groups ($0.86 \leqslant x^0_{\mathrm{P}} \leqslant 0.96$), with the remaining constituting Q^1_{P} moieties. To assist comparisons with the YDBX[37,38] prediction of the $B^{[3]}/B^{[4]}$ partitioning, we introduce the ratio $R' = x(\mathcal{M}_2\mathrm{O})/x(\mathrm{B_2O_3}) = x_{\mathcal{M}}/x_{\mathrm{B}}$ that accounts for the consumption of Na^+/Ca^{2+} ions required to charge-balance all $\{Q^0_{\mathrm{P}}, Q^1_{\mathrm{P}}\}$ phosphate groups by considering the *fictive* monovalent ion $\mathcal{M}^+$, whose content relates to the net amount of positive charges available for the B/Si species of the *borosilicate* network, according to

$$x_{\mathcal{M}} = x_{\mathrm{Na}} + 2x_{\mathrm{Ca}} - x_{\mathrm{P}}(3x^0_{\mathrm{P}} + 2x^1_{\mathrm{P}}). \tag{1}$$

Consequently, each Na_2O–CaO–B_2O_3–SiO_2–P_2O_5 glass composition $SN_p(q)$ maps onto a $\mathcal{M}_2O$–

B_2O_3–SiO_2 counterpart associated with the parameter R' that may be contrasted directly with the result of a Na_2O–B_2O_3–SiO_2 analog with $R = x(Na_2O)/x(B_2O_3)$ and $K = x(SiO_2)/x(B_2O_3)$ from the YDBX model.[37,38] Table **1** lists the resulting values of R', K, and other relevant glass composition factors, such as x_B/x_{Si}.

Note that this simplistic picture only accounts for the *total* positive charge reservoir provided from the monovalent Na^+ and divalent Ca^{2+} cations. In our previous studies of ^{31}P and ^{29}Si environments in phosphosilicate glasses,[33–35] no significant differences were observed from slight variations in the relative Na/Ca contents among different glasses, where the main glass-network alterations are captured well by solely considering the total glass modifier content, the P content, and the silicate network connectivity. Also for the present BPS glasses, the minor difference among the x_{Na}/x_{Ca} ratios of the S46 and S49 families is not expected to alter the glass structures significantly; indeed, we verified for two S49 members that the two x_{Na}/x_{Ca} values of 1.84 and 2.08 yield $B^{[4]}$ fractional populations that agree within 97% [for $S49_{4.0}(15)$] and 99% [for $S49_{4.0}(24)$]. While such minor differences are immaterial for any result discussed herein, further studies are required to assess the precise structural bearings from the relative amounts of Na^+ and Ca^{2+} (if any), as well as their influences on the *in vitro* glass degradation and bioactivity.

3 Materials and Methods

3.1 Glass Preparation and Characterization

6.0 g batches of the BPS glasses were prepared by a standard melt-quench method, using precursors of SiO_2 (99.99%), Na_2CO_3 (99.99%), and $CaCO_3$ (99.9%) from ChemPur, and NaH_2PO_4 (99.99%, Merck), and H_3BO_3 (99.9%, Sigma). Prior to its weighing, the SiO_2 powder was heated at 950 °C for 24 h to remove potential OH/H_2O contaminations. The precursors were ground, weighted, and transferred to a bottle that was shaken thoroughly before another mixing stage in a mortar for 1

hour to achieve homogeneous powders. The mixture was then placed in a Pt crucible and heated in an electric furnace at 950 °C for 120 min to allow for complete CO_2 removal. Depending on the P_2O_5 and SiO_2 contents of each batch, the temperature was then increased to 1200–1250 °C (S46 series) and 1300–1400 °C (S49 series), held for 20 min (S46 specimens) or 30 min (S49), before quenching the melt by immersing the bottom of the crucible in water.

The evaporation losses during synthesis remained $\lesssim$1.5 wt% throughout. We verified by ^{11}B MAS NMR on two specimens [$S46_{2.6}(28)$ and $S46_{2.6}(37)$] that insignificant alterations in the peak-shapes and NMR intensities resulted after repeating the melt-quench process on the initially prepared glasses. Besides confirming sufficient precursor mixing, it strongly suggests very limited evaporation losses of the most volatile glass ingredient (*i.e.*, B). Moreover, the relative integrated ^{31}P NMR intensities (section 4.1) among the samples were in excellent agreement with the corresponding nominal $x(P_2O_5)$ values, thereby further suggesting intact batch compositions.

Polished glass samples were coated by a 10–20 nm thick carbon layer and examined by scanning electron microcopy (SEM), using a JEOL JSM-7000F microscope in backscatter electron mode at a 15 kV acceleration voltage. None of the specimens manifested signatures of phase separation down to the shortest accessible length-scale of 1 μm.

3.2 Solid-State NMR

All NMR experiments utilized Bruker Avance-III spectrometers. The ^{31}P and ^{29}Si MAS NMR spectra were recorded at a magnetic field (B_0) of 9.4 T, which corresponds to ^{31}P and ^{29}Si Larmor frequencies of −162.0 MHz and 79.5 MHz, respectively. Glass powder were filled in 7 mm zirconia rotors that were spun at 7.00 kHz during the NMR signal acquisitions. All ^{11}B NMR experimentation was performed at B_0 =14.1 T (−192.5 MHz ^{11}B Larmor frequency) with 3.2 mm rotors spinning at 24.00 kHz.

The ^{31}P and ^{29}Si NMR acquisitions were performed in blocks, using single-pulse excitation with flip angles of 70° (^{31}P) or 60° (^{29}Si) at radio-frequency (rf) nutation frequencies $\nu_{\rm nut} = |\gamma|\, B_1/2\pi \approx$ 60 kHz, where B_1 is the rf amplitude. The ^{31}P NMR acquisitions involved ≈48 accumulated signal transients, with 5000 s "equilibration" delays before the start of each block of 8 transients, and relaxation delays of 2500 s between each rf pulse within the block. Depending on the Si content of the glass, between 92–156 transients were recorded with 3600 s relaxation delays and equilibration delays of 3.5 h between each block of 4-8 transients. 300 Hz and 200 Hz full width at half maximum (fwhm) height Gaussian broadening were employed in the ^{29}Si data processing of the S46 and S49 glasses, respectively, whereas no signal apodization was employed for the ^{31}P NMR data.

^{11}B MAS NMR data were recorded using short (0.5 μs; ≈15°) rf pulses at $\nu_{\rm nut} \approx$ 75 kHz, relaxation delays of 15 s, and 512–3072 accumulated transients, depending on the B content of the sample. ^{11}B background signals from the MAS NMR probehead were removed by subtracting the results from an empty rotor. No signal apodization was used in the processing, except for the $S49_{4.0}(2)$ glass that employed 225 Hz fwhm Gaussian broadening.

Triple quantum MAS (3QMAS)[57] ^{11}B NMR acquisitions employed the Z-filter scheme[58,59] utilizing the symmetric $0 \rightarrow \pm 3 \rightarrow \pm 1 \rightarrow 0 \rightarrow -1$ quantum coherence pathways. All rf pulses for 3Q coherence (3QC) excitation and conversion operated at $\nu_{\rm nut}$=115 kHz. The 3QC excitation pulse lasted for 5.8 μs. Two FAM[60] blocks with equal durations of the pulses and delays of 0.90 μs were used for the $\pm 3 \rightarrow \pm 1$ coherence transfer. The two central transition (CT) selective 90° pulses of duration 17.0 μs ($\nu_{\rm nut}$ =7.4 kHz) following the 3QC conversion were interleaved by a Z-filter delay of one rotational period. The 2D NMR acquisitions involved the States procedure[61] for providing absorptive peaks with frequency sign-discrimination along the indirect spectral dimension, together with dwell times $\{\triangle t_1, \triangle t_2\}$={41.7, 6.1} μs, 2 s relaxation delays, and 288–3456 co-added transients. Typically, $100(t_1)\times 2428(t_2)$ time-points were recorded and zero-filled to 512×8192 points.

The indirect 3QMAS dimension was processed according to the "C_z" convention.[57,62]

These experimental conditions—i.e., the flip angles, "pre-equilibration" and "relaxation" (or "interpulse") delays—were selected for each nucleus from separate saturation-recovery T_1 measurements to ensure NMR data quantitatively reflecting the populations of the various B, Si and P structural sites. ^{31}P, ^{11}B, and ^{29}Si shifts are quoted relative to 85% H_3PO_4(aq), neat $BF_3{\cdot}OEt_2$, and neat tetramethylsilane (TMS), respectively; the liquids were also exploited for estimating rf nutation frequencies, except for the ^{31}P rf pulses that were calibrated directly on the glass samples.

4 Results

4.1 ^{31}P MAS NMR

The ^{31}P MAS spectra recorded from the S46 and S49 glass families are shown in Fig. **1**. The two base glasses, $S46_{2.6}(0)$ and $S49_{4.0}(0)$, reveal peak maxima at 8.7 ppm and 8.3 ppm, respectively, corresponding to signals from *ortho*phosphate groups charge-balanced by Na^+/Ca^{2+} cations.[22,30–34,63] The marginally lower shift of the NMR peak from the $S49_{4.0}(0)$ glass, which features slightly higher x_{Na}/x_{Ca} ratio and $\overline{N}^{Si}_{BO}$ value, stems from two counteracting factors: the deshielding effect of Na^+ (relative to Ca^{2+}) that *increases* the shift,[22,30,33,34,63] and the shielding (shift reduction) resulting from emphasized Ca^{2+}–PO_4^{3-} associations when $\overline{N}^{Si}_{BO}$ grows.[34] The large fwhm of the NMR peaks ≈7.5 ppm reflect the disordered glass structures. The ^{31}P resonances of $S46_{2.6}(0)$ are characterized by a nearly Gaussian peakshape, while that for $S49_{4.0}(0)$ appears more asymmetric, featuring a "tail" towards lower shifts: it stems from Q^1_P moieties, *i.e.*, phosphate groups with one P–O–**Si** (as *opposed* to P–O–**P**) bond.[32–34,36,64,65] For both S46 and S49 series, Fig. **1** reveals progressively more asymmetric ^{31}P resonances for increasing $x(B_2O_3)$ in the glass. While the the growing amount of Q^1_P species may *potentially* involve *either* of P–O–**Si**/**B** bonding scenarios, additional heteronuclear ^{31}P{^{11}B} NMR experiments (to be published elsewhere) suggest that few P–O–**B**

bonds form and that P–O–**Si** bridges prevail, as in the parent B-free phosphosilicate glasses.

To quantify the influence of the increased B_2O_3 content on the phosphate speciation, we deconvoluted each ^{31}P NMR peak into two Gaussian components by a constrained iterative fitting, considering both the centerband and first-order spinning sidebands stemming from each Q^0_P/Q^1_P group (see Mathew *et al.*[33]). Each peak component was represented by three parameters, $\{\delta^n_P$, W^n_P, $x^n_P\}$, corresponding to the mean ^{31}P chemical shift (δ^n_P), the fwhm (W^n_P), and the fractional population (x^n_P). Table **2** lists the best-fit results. For both the S46/S49 glass series, the chemical shift of the orthophosphate groups (δ^0_P) decreases congruently with the respective maximum of the net NMR signal, suggesting a more pronounced propensity for the Q^0_P groups to associate with the Ca^{2+} cations relative to Na^+.[33,34,36] The more than twice as large x^1_P population (≈10%) of the $S49_{4.0}(0)$ structure relative to its $S46_{2.6}(0)$ counterpart is consistent with its larger $\overline{N}^{Si}_{BO}$ value and the linear $\overline{N}^{Si}_{BO}/x^1_P$ relationship established recently by Mathew *et al.*[33] When the B_2O_3 content grows, a weak increase of x^1_P is observed between 0.041–0.065 (for S46) and 0.100–0.136 (for S49), which reflect minor increases of the silicate network polymerization, as discussed in section 4.2.

4.2 ^{29}Si MAS NMR

The ^{29}Si chemical shift of a Q^n_{Si} group in a silicate glass depends essentially on the same structural factors as ^{31}P in phosphate glasses (see section **4.1**), *i.e.*, on the relative number of BO/NBO species at the SiO_4 tetrahedron (n) and the precise Na^+/Ca^{2+} constellation that provides local charge balance.[1–3,40,66,67] However, in a multicomponent glass—such as the present Na_2O–CaO–SiO_2–P_2O_5 specimens $S46_{2.6}(0)$ and $S49_{4.0}(0)$—the BO/NBO distribution, variations in the relative numbers of Na^+/Ca^{2+} cations around each SiO_4 group, and distributions in Si–O bond lengths and Si–O–Si bond angles give a plethora of co-existing local ^{29}Si environments with similar chemical shifts that preclude the identification of the responses from individual Q^n_{Si} species.[1–3,40]

Figure **2**(a, b) presents the ^{29}Si MAS NMR spectra of the two B-free $S46_{2.6}(0)$ and $S49_{4.0}(0)$ glasses. Consistent with the expected domination of Q^2_{Si} groups in the $S46_{2.6}(0)$ structure ($\overline{N}^{Si}_{BO}$=2.11), its ^{29}Si NMR peakshape is nearly Gaussian. However, a "tail" towards lower shifts is discernible, signifying the presence of Q^3_{Si} groups resonating at lower chemical shifts ≈ -88 ppm. Their larger contributions to the more polymerized silicate network of the $S49_{4.0}(0)$ glass is evident from its NMR peakshape that corresponds to a superposition of (mainly) two Gaussian peaks centered around -80 ppm (Q^2_{Si}) and -88 ppm (Q^3_{Si}).

Figure **2**(a, b) also displays the deconvolution of each NMR spectrum into its underlying $\{Q^n_{Si}\}$ peak components, where the results for $S46_{2.6}(0)$ are reproduced from Mathew *et al.*[33] Q^2_{Si} groups ($\approx$72%) dominate the silicate speciation of the $S46_{2.6}(0)$ structure, as expected from its nominal silicate network connectivity of 2.11. Indeed, the best-fit $\{x^1_{Si}, x^2_{Si}, x^3_{Si}\}$ populations together with the expression

$$\overline{N}^{Si}_{BO} = \sum_n n x^n_{Si}, \tag{2}$$

provided the experimental estimate $\overline{N}^{Si}_{BO}$=2.14;[33] see Fig. **2**(a). The respective $\{x^1_{Si}, x^2_{Si}, x^3_{Si}, x^4_{Si}\}$ values of $S49_{4.0}(0)$ are {0.015, 0.403, 0.571, 0.011}, corresponding to $\overline{N}^{Si}_{BO} = 2.58$ and in excellent agreement with the nominal value $\overline{N}^{Si}_{BO}$=2.54. These populations accord well with those of the B-free Na–Ca–Si–P–O "$BG_{4.0}(2.5)$" glass discussed in ref.[33] that is associated with $\overline{N}^{Si}_{BO} = 2.50$. The present $S49_{4.0}(0)$ composition features very close SiO_2 and P_2O_5 contents to $BG_{4.0}(2.5)$, with the main distinction being their different Na/Ca contents, where $S49_{4.0}(0)$ is richer in Na (x_{Na}/x_{Ca}=2.08) relative to $BG_{4.0}(2.5)$ with $x_{Na}/x_{Ca} = 1.54$.

Figure **2**(c, d) displays the ^{29}Si NMR spectra of the B-bearing members of each S46/S49 glass family. Only minor resonance-alterations are observed when SiO_2 is substituted by B_2O_3. Notably, the NMR peak maxima from all S46 glasses remain ≈ -80 ppm for $x(B_2O_3)\leqslant 0.28$, where only the B-richest glass reveals a noticeable peak displacement to -78.6 ppm. Likewise, all S49-deriving

glasses manifest equal peak maxima ≈ -83 ppm, with their main distinctions being a reduced signal intensity in the low-ppm region ≈ -90 ppm as the B content is increased. Two factors may account for the minor increase of the ^{29}Si chemical shifts when B is included in the glass structure:

(*i*) The silicate network polymerization decreases slightly, such that lower-n Q^n_{Si} populations grow, thereby inducing a ^{29}Si deshielding with a typical shift displacement of 7–12 ppm per $Q^n_{\mathrm{Si}} \rightarrow Q^{n-1}_{\mathrm{Si}}$ transformation.[1–3,66,67] However, this implies an *increase* of the average number of NBO species at the SiO_4 groups. This scenario is precluded by the constant Na^+/Ca^{2+} content of the glasses of each S46/S49 series: after accounting for the modifier consumption by the phosphate and $[BO_4]^-$ species, the BO_3 groups may also accommodate NBO ions and therefore an *increase* (rather than a decrease) of the silicate network polymerization is anticipated.

(*ii*) Substitutions of Si by B$^{[4]}$ species in the second coordination shell of ^{29}Si typically induce ≈5 ppm ^{29}Si deshielding per ^{29}Si–O–**Si**→^{29}Si–O–**B**$^{[4]}$ conversion,[1–3,39,45–47] whereas the ^{29}Si–O–**Si**→^{29}Si–O–**B**$^{[3]}$ replacements preserve the net charge of the O atom, thereby leaving the ^{29}Si chemical shift value essentially invariant.[43,45–47] While it is then tempting to interpret the minor alterations of the ^{29}Si NMR spectra in Fig. **2** to reflect a predominance of Si–O–B$^{[3]}$ bonds,[39] this scenario is excluded from the ^{11}B NMR results discussed in sections **4.3** and **5.1**.

Most likely, the weak but clearly discernible deshielding of the ^{29}Si nuclei reflects the net effect of the two opposing factors (*i*) and (*ii*), *i.e.*, the shift *elevation* from the neighboring B$^{[4]}$ atoms is partially offset by a slight shift *reduction* from a higher $\overline{N}^{\mathrm{Si}}_{\mathrm{BO}}$ value. The enhanced Si/B intermixing leads to a larger shift *dispersion* stemming from a plethora of ^{29}Si environments featuring variable number of Si–O–B$^{[4]}$ bonds;[40,45–47] see Fig. **2**(d). The ^{29}Si resonance-broadening and overall loss of peakshape features for increasing B_2O_3 content is well documented: for instance, see Fig. 3 of El-Damrawi *et al.*[46] and Fig. 4 of Edén *et al.*[40] Owing to the multitude of potentially co-existing but unresolved ^{29}Si NMR responses, spectra deconvolutions are unfortunately not warranted for the B-

bearing glasses. However, given the absence of significant ^{31}P–O–B contacts (section **4.1**) coupled with the linear dependence of the Q^1_P population on the average silicate network connectivity,[33] we may estimate $\overline{N}^{Si}_{BO}$ from the x^1_P-values of Table **2** and the quantitative $x^1_P/\overline{N}^{Si}_{BO}$ relationship established by Mathew *et al.*[33] Across the S46 glass series, the growth of x^1_P from 0.041 to 0.065 then translates into a minor increase of $\overline{N}^{Si}_{BO}$ from 2.11 to ≈2.24, while the S49 glasses yield the corresponding $\overline{N}^{Si}_{BO}$ growth from 2.54 to 2.73. Hence, when the B_2O_3 content of the glass elevates, the silicate network polymerization increases slightly, while the ^{29}Si sites become slightly deshielded by the formation of Si–O–B$^{[4]}$ bonds. The observation of a nearly constant silicate network polymerization on B↔Si substitutions at a constant modifier content accords with the recent findings by Smedskjaer et al.[53] for more condensed borosilicate networks.

4.3 ^{11}B NMR

4.3.1 MAS NMR

Figure **3** shows a selection of ^{11}B MAS NMR spectra from each S46 and S49 glass family. The spectra are zoomed around the CT signal region and reveal two groups of resonances: a broad signal from $^{11}BO_3$ groups, and a narrow asymmetric Gaussian peak from the $^{11}BO_4$ tetrahedra. The latter exhibits lower average quadrupolar coupling constants ($\overline{C}_Q$, with C_Q=e^2qQ/h) owing to the higher symmetry of the charge distribution around the ^{11}B nucleus.[37,38,46,47] The following general trends are observed in Fig. **3** when SiO_2 is substituted by B_2O_3 at a constant network modifier content: (*i*) The intensity of the ^{11}B$^{[4]}$ resonance increases due to B$^{[3]}$ →B$^{[4]}$ conversions,[37,38,45,47] while its position displaces monotonically towards higher shifts. As analyzed further in section **5.1**, this reflects a concurrent decrease in the number of Si atoms in the second coordination shell of ^{11}B.[44,45,49–52] (*ii*) The ^{11}B$^{[3]}$ resonance alters from an essentially featureless peak, centered at 13.9 ppm (S46) and 13.3 ppm (S49) from the Si-rich glass compositions, to a broad signal revealing two

maxima ≈15.8 ppm and ≈12.5 ppm; see Fig. **3.** This suggests that the ^{11}B NMR signals in the ≈8–20 ppm spectral region stem from at least two distinct $^{11}BO_3$ environments in all Si-dominated glasses, as discussed further below.

The $\{x_B^{[3]}, x_B^{[4]}\}$ populations were determined from the integrated CT NMR signal intensities of the respective $\{^{11}BO_3, ^{11}BO_4\}$ groups, including the weak first-order $^{11}BO_3$ CT spinning sidebands. Each $^{11}BO_4$ intensity was corrected for the contributions of the ST centerband (which overlap with the main CT resonance) according to the procedure of Massiot *et al.*;[68] the correction yielded 0.02–0.03 lower $x_B^{[4]}$ values relative to the corresponding uncorrected populations. The results are listed in Table **3**, together with the mean isotropic chemical shifts and average quadrupolar products $\overline{C}_{Q\eta}$ of the $^{11}BO_4$ moieties ($C_{Q\eta}$ relates to C_Q according to $C_{Q\eta}$=$C_Q\sqrt{1+\eta^2/3}$, where η is the asymmetry parameter of the quadrupolar tensor[1–3]). These parameters were obtained by analyzing the CT/ST signals of the ^{11}B MAS NMR spectra as described in ref.[69] We stress that all $\{\overline{\delta}_{iso}, \overline{C}_{Q\eta}\}$ parameters listed in Table **3** are mean values of (up to) three co-existing $^{11}BO_4$ environments with variable numbers of Si/B$^{[3]}$ neighbors (see section **5.1**), whose individual NMR parameters cannot be determined.

Figure **4** plots the B$^{[4]}$ fractional population ($x_B^{[4]}$) against $x(B_2O_3)$. Both S46/S49 series reveal a strong growth of $x_B^{[4]}$ when $x(B_2O_3)$ is increased at low substitution levels [$x(B_2O_3)\lesssim$0.07]. When the amount of B is elevated further, $x_B^{[4]}$ tends towards asymptotic values of ≈0.34 and ≈0.43 for the S46 and S49 glass families, respectively. However, while the plateau is reached at already ≈30% B_2O_3 for SiO_2 substitution of the S49 glasses, the B$^{[4]}$ population manifests a slow increase throughout the entire range of B_2O_3 contents in the S46 series. Noteworthy, the increase of $x_B^{[4]}$ (by ≈17%) across the S46 glasses is more than twice that (≈7%) observed for the S49 members. As expected from the ^{11}B$^{[4]}$ peak intensities of Fig. **3**, the overall Si-richer S49 glasses exhibit higher relative B$^{[4]}$ populations than their S46 counterparts. While this trend is predicted by the YDBX

model,[37,38] it accounts only qualitatively for the *de-facto* observed alterations of the experimental $B^{[4]}$ populations for variable amounts of B; see Fig. **4**.

4.3.2 3QMAS NMR

Since it removes the anisotropic second-order quadrupolar broadenings, the 3QMAS 2D NMR technique[57] improves the ^{11}B NMR spectral resolution by producing a high resolution "isotropic" (indirect) dimension. The direct ("MAS") dimension essentially retains the MAS NMR spectrum. In the isotropic projection of 3QMAS data from glasses, the residual peak broadening stems mainly from isotropic chemical-shift distributions due to the structural disorder.[3,59,70] Figure **5**(a) displays the 3QMAS ^{11}B NMR spectrum together with its projections along each isotropic/MAS dimension from the Si-rich $S46_{2.6}(9)$ glass. The NMR spectrum reveals two well-separated 2D "ridges" of resonances from $^{11}B^{[4]}$ and $^{11}B^{[3]}$ structural sites that extend along both spectral dimensions: the two arrows shown in Figure **5**(a) represent the directions of signal dispersion stemming from the respective spreads of isotropic chemical shifts and C_Q values.[70]

Figure **5**(b, c) shows zoomed areas around the $^{11}B^{[3]}$ 2D NMR ridge, where pairs of spectra from glasses with low and high amounts of B are superimposed from the (b) S46 and (c) S49 glass series. Each Si-dominated glass reveals a higher NMR signal-dispersion towards lower shifts relative to its B-richer counterparts: it is manifested by an enhanced NMR intensity $\approx$ 74 ppm in the corresponding projection along the isotropic dimension and suggests that the net $^{11}B^{[3]}$ resonance stems from *two* (or more) distinct BO_3 structural environments. This is most transparent for the two S46 samples that exhibit the largest span of B contents; see Fig. **5**(b).

The correlation between the signal intensity $\approx$74 ppm and the relative SiO_2 content of the glass is evident from the isotropic projections shown in the left panel of Fig. **6**. The ^{11}B NMR peakshape from the almost Si-free $S46_{2.6}(37)$ glass fitted well to a single Gaussian peak centered

≈82 ppm [Fig. **6**(a)], indicating that its structure comprises primarily *one* type of BO_3 structural group. Given the domination of B relative to Si in the glass network (x_B/x_{Si} =8.00; see Table **1**), we attribute it to a BO_3 environment participating in boroxol rings[50–52,55] and devoid of bonds to Si atoms; this moiety is consequently labeled $B^{[3]}$(0Si). The lower-ppm signal grows for increasing SiO_2 content, indicating it is associated with a "non-ring" BO_3 environment connected to one SiO_4 group, which we denote by $^{11}B^{[3]}$(1Si).

The relative $^{11}B^{[3]}$(0Si) ["ring"] and $^{11}B^{[3]}$(1Si) ["non-ring"] contributions were extracted by deconvoluting each NMR spectrum into two components; see Fig. **6**. The variable $^{11}B^{[3]}$(0Si) and $^{11}B^{[3]}$(1Si) peak intensities are responsible for the lineshape alterations of the MAS spectra in Fig. **3** when the x_B/x_{Si} ratio of the glass is changed. The $B^{[3]}$(1Si) population grows up to 24% when $x(B_2O_3)$ is decreased from 0.37 to 0.09 in the S46 series; it amounts to 30% out of the total $B^{[3]}$ speciation in the Si-richest glass [$S49_{4.0}(10)$] that was examined by 3QMAS ^{11}B NMR; see Fig. **6**(i). As follows by comparing the results for $S46_{2.6}(9)$ and $S49_{4.0}(10)$ that feature a constant B_2O_3 for SiO_2 substitution degree of 20%, the $B^{[3]}$(1Si) contribution is larger for the Si-richer BPS glass with *lower* NBO content. These trends of growing "non-ring" fraction for increasing (decreasing) amount of Si (NBO) accord with the results of Du and Stebbins for alkali-poor borosilicate glasses.[50,51]

5 Discussion

5.1 BO_4 Environments

5.1.1 $B^{[4]}$–O–B/Si Bond Statistics

The $^{11}BO_4$ NMR peak displacements towards higher chemical shifts for increasing B_2O_3 content (Fig. **3**; Table **3**) reflect progressive $B^{[4]}$–O–**Si**→$B^{[4]}$–O–$\mathbf{B}^{[3]}/\mathbf{B}^{[4]}$ substitutions. Net NMR peak movements of ≈1 ppm are observed across both glass series, while the present ^{11}B CG shifts are

overall higher than those of the mainstream borosilicate studies that generally targeted Si-richer glasses with relatively low modifier contents, $x(M_{(2)}\mathrm{O}) \lesssim 0.3$.[39,43,46,47,50–54,69]

Given that the total Na^+/Ca^{2+} content remains *constant* within each S46 and S49 series, the $^{11}B^{[4]}$ resonance-displacement may be accounted for by a fixed set of groups, $\{^{11}B^{[4]}(m\mathrm{Si})\}$, each featuring m bonds to Si atoms (and thereby $4-m$ bonds to $B^{[3]}$) and resonating at the CG shift $\delta_B^{[4]}(m\mathrm{Si})$. Several investigations report a propensity for BO_4 groups to connect to SiO_4 tetrahedra rather than the planar BO_3 moieties,[37,38,50–52] whereas direct $B^{[4]}$–O–$B^{[4]}$ linkages are often assumed to be absent in the borosilicate structure.[1–3,37,38,50–52] Hence, $B^{[4]}$(4Si) environments are expected to dominate the BO_4 speciation in the Si-richest BPS glasses. Yet, considering the wide ranges of x_B/x_{Si} ratios sampled across the S46/S49 glass series (notably so for the S46 set; see Table **1**), more than two structural moieties should co-exist: with the constraints of combining physically reasonable $\{\delta_B^{[4]}(m\mathrm{Si})\}$ values with decent "best fits", three $\{^{11}B^{[4]}(4\mathrm{Si}),\ ^{11}B^{[4]}(3\mathrm{Si}),\ ^{11}B^{[4]}(2\mathrm{Si})\}$ groups were selected and each $^{11}BO_4$ NMR signal of Fig. **3** was deconvoluted into Gaussian-shaped peaks centered at the nearly constant ($\pm$0.1 ppm) shift-values $\{-0.45, 0.65, 1.85\}$ ppm for all glasses. We stress that these NMR spectra deconvolutions are somewhat arbitrary because the set of precise $\{\delta_B^{[4]}(m\mathrm{Si})\}$ values are *a priori* unknown. The proposed shift alteration associated with a $B^{[4]}(m\mathrm{Si}) \rightarrow B^{[4]}([m-1]\mathrm{Si})$ conversion varies between various studies, where (for instance) shift differences of 0.7–1.0 ppm,[47,71] and 1.7–2.0 ppm[51,52] are suggested.

Figure **7** presents the set $\{x_B^{[4]}(m\mathrm{Si})\}$ of best-fit fractional populations plotted against each ratio

$$y_B = x_B/(x_B + x_{Si}), \tag{3}$$

and

$$y_B^{[3]} = x_B x_B^{[3]}/(x_B x_B^{[3]} + x_{Si}), \tag{4}$$

in the left and right panels, respectively. When employing y_B, no distinction is made between the two $B^{[3]}/B^{[4]}$ coordinations, whereas the ratio $y_B^{[3]}$ is relevant for the scenario of $B^{[4]}$–O–$B^{[4]}$ avoidance, where $y_B^{[3]}$ represents the fraction of BO_3 groups out of the total number of BO_3/SiO_4 species available for bonding to the BO_4 tetrahedra. Note that depending on whether Eq. (3) or Eq. (4) is considered, y_{Si} obeys $y_{Si}=1-y_B$ and $y_{Si}=1-y_B^{[3]}$, respectively. At low B substitution levels, $x(B_2O_3)\lesssim 0.05$, the BO_4 groups enter the glass structure predominantly as $B^{[4]}$(4Si) environments, while the $B^{[4]}$(3Si) population accounts for $\lesssim$20% out of the total $B^{[4]}$ speciation and the fraction of $B^{[4]}$(2Si) moieties remains $x_B^{[4]}(2Si)<0.1$; see Fig. **7**(a–d). For increasing B_2O_3 content, the progressive $B^{[4]}(4Si)\rightarrow B^{[4]}(3Si)\rightarrow B^{[4]}(2Si)$ conversions imply that BO_4 groups with three bonds to Si prevail for $x(B_2O_3)\gtrsim 0.14$, *i.e.*, when $\gtrsim$30% of SiO_2 is replaced by B_2O_3. In the B-richest $S46_{2.6}(37)$ structure, similar populations of $B^{[4]}$(3Si) and $B^{[4]}$(2Si) environments co-exist, whereas the $B^{[4]}$(4Si) species only represent ≈9% of all BO_4 groups; see Fig. **7**(a, b).

5.1.2 Quantifying the Preference for $B^{[4]}$–O–Si Bonds

Figure **7**(e, f) displays the $x(B_2O_3)$-dependence of the average number of Si atoms in the second coordination sphere of $B^{[4]}$: $\overline{N}_{Si} = \sum_m m x_B^{[4]}(m\text{Si})$. The corresponding average number of B atoms ($\overline{N}_B$) is given from the constraint $\overline{N}_B=4-\overline{N}_{Si}$, where "B" represents the *total* B speciation in Fig. **7**(e) but *solely* the $B^{[3]}$ coordinations in (f). The mean number of Si neighbors around the BO_4 groups decreases from $\overline{N}_{Si}=3.62$ in the Si-rich $S46_{2.6}(5)$ structure to $\overline{N}_{Si}=2.70$ in the B-rich $S46_{2.6}(37)$ glass. The corresponding data observed for the S49 series are $\overline{N}_{Si}=3.94$ [$S49_{4.0}(2)$] and $\overline{N}_{Si}=2.95$ [$S49_{4.0}(24)$]. These overall high $\overline{N}_{Si}$-values underscore the preference for $B^{[4]}$–O–**Si** contacts relative to $B^{[4]}$–O–**B**. This inference is obvious when contrasting the experimentally observed $\{\overline{N}_{Si}\}$ data with the scenario of random distributions of either the $Si/B^{[3]}$ species [Fig. **7**(f)] or of *all* $Si/B^{[3]}/B^{[4]}$ moieties [Fig. **7**(e)] around the BO_4 groups. Besides that the statistical

(binomial) distribution reveal a markedly faster drop of $\overline{N}_{\mathrm{Si}}$ than that observed experimentally, it leads to substantial $\{x_{\mathrm{B}}^{[4]}(0\mathrm{Si}),\ x_{\mathrm{B}}^{[4]}(1\mathrm{Si})\}$ populations (data not shown) that are incommensurate with the experimental observation of (up to) three co-existing $\mathrm{B}^{[4]}(m\mathrm{Si})$ structural groups.

To asses the *degree* of *preference* for $\mathrm{B}^{[4]}$–O–**Si** bond formation relative to $\mathrm{B}^{[4]}$–O–**B**, we employed the procedure introduced recently by Mathew *et al.*[34] It applies to a scenario where two distinct atom species V and W may be coordinated by U: when there is a preference for U–V contacts, the *preference factor* P_V—where the subscript "V" denotes the *preferred* species—encodes the deviation from a statistical V/W distribution around U (for which P_V=P_W=0), where P_V=1 represents the case of *sole* U–V bonding. Within this framework, the preference factor P_{Si} dictates the *average number* of Si ($\overline{N}_{\mathrm{Si}}$) and B ($\overline{N}_{\mathrm{B}}$) atoms around the $\mathrm{B}^{[4]}$ coordinations as follows:[34]

$$\overline{N}_{\mathrm{Si}} = 4[P_{\mathrm{Si}} + y_{\mathrm{Si}}(1 - P_{\mathrm{Si}})], \tag{5}$$

$$\overline{N}_{\mathrm{B}} = 4y_{\mathrm{B}}(1 - P_{\mathrm{Si}}) \quad \text{for equal } \mathrm{B}^{[3]}/\mathrm{B}^{[4]} \text{ probabilities} \tag{6}$$

$$= 4y_{\mathrm{B}}^{[3]}(1 - P_{\mathrm{Si}}) \quad \text{for } \mathrm{B}^{[4]}\text{–O–}\mathrm{B}^{[4]} \text{ avoidance,} \tag{7}$$

where y_{B} and $y_{\mathrm{B}}^{[3]}$ are given by Eq. (3) and (4), respectively. Depending on whether $\mathrm{B}^{[4]}$–O–$\mathrm{B}^{[4]}$ contacts are allowed [Eq. (6)] or forbidden [Eq. (7)], the total $\mathrm{BO_3}/\mathrm{BO_4}$ ensemble or solely the $\mathrm{BO_3}$ groups contribute to $\overline{N}_{\mathrm{B}}$.

For each glass, the preference for $\mathrm{B}^{[4]}$–O–Si bonds was calculated from the experimental data of Fig. **7**(a–d) by using Eq. (5) and solving for P_{Si}. Onwards disregarding the result for the Si-richest $\mathrm{S49}_{4.0}(2)$ glass that is considered to be an outlier, no striking differences are observed if $\mathrm{B}^{[4]}$–O–$\mathrm{B}^{[4]}$ linkages would be absent or present, with the respective $\{P_{\mathrm{Si}}\}$ data typically scattering around

the values 0.45 and 0.55. Consequently, the scenario of $B^{[4]}$–O–$B^{[4]}$ avoidance is associated with a somewhat less pronounced propensity for $B^{[4]}$–O–Si bond formation; this is evident from Fig. **7**(e, f), where the experimental $\overline{N}_{Si}$ values of nearly all members from the S46 and S49 families are bracketed by the results stemming from distribution models associated with P_{Si}=0.60 and the corresponding lower limit of P_{Si}=0.40 if $B^{[4]}$–O–$B^{[4]}$ bonds are allowed [Fig. **7**(e)] and P_{Si}=0.20 when $B^{[4]}$–O–$B^{[4]}$ links are absent [Fig. **7**(f)].

To conclude, the BO_4 moieties in both S46 and S49 glass families display a clear preference for connecting to SiO_4 tetrahedra rather than to BO_3/BO_4 groups. The observed typical values of P_{Si} ≈0.5 are equivalent to a Si/B distribution where Si atoms first occupy two out of four positions at each BO_4 tetrahedron, whereas Si and B atoms are statistically distributed at the remaining two tetrahedral corners. However, considering the uncertainties and possible systematic errors of the experimental $\overline{N}_{Si}$-data, the precise values should not be taken too literally and further studies are required to better confine the relative preferences, as well as if "$B^{[4]}$ avoidance" applies to modifier-rich BPS glass networks.

5.2 NBO Partitioning Among SiO_4 and BO_3 Groups

The affinity for coordinating NBO ions among the three {P, Si, B} network formers decreases in the order P≫Si>$B^{[3]}$ ≫$B^{[4]}$.[3,40] Because $B^{[4]}$–NBO bonds are assumed to be absent[3,40] and the NBO accommodation among the Q^0_P (PO_4^{3-}) and Q^1_P ($PO_{3.5}^{2-}$) moieties are known accurately (see Table **2**), we henceforth focus on the NBO partitioning among the SiO_4 and BO_3 groups.

The *total* NBO population available for depolymerizing the borate/silicate networks may be estimated for each glass after accounting for the consumption of Na^+/Ca^{2+} cations by the phosphate groups [see eq. (1)] and the $[BO_4]^-$ tetrahedra. By using the average *silicate* network connectivity ($\overline{N}^{Si}_{BO}$) available from the Q^1_P population (section **4.2**), the mean numbers of BO ($\overline{N}^{B}_{BO}$) and

NBO ($\overline{N}^{\mathrm{B}}_{\mathrm{NBO}}$) species at the BO_3 groups may be estimated. The S46 and S49 glasses exhibit relatively narrow $\overline{N}^{\mathrm{Si}}_{\mathrm{NBO}}$ ranges of 1.76–1.89 and 1.27–1.46, respectively, yielding the corresponding *approximate* $\overline{N}^{\mathrm{B}}_{\mathrm{NBO}}$-values of 1 and 0.7–0.8. Hence, the $\{\overline{N}^{\mathrm{B}}_{\mathrm{NBO}}, \overline{N}^{\mathrm{Si}}_{\mathrm{NBO}}\}$ parameter-pair only alters slightly across each S46/S49 glass family when the $x_{\mathrm{B}}/x_{\mathrm{Si}}$ ratio varies. It is instructive to compare the results conveying the relative propensities for Si–NBO and $B^{[3]}$–NBO bond formation between the two series, which reveal the pairs $\{\overline{N}^{\mathrm{B}}_{\mathrm{NBO}}, \overline{N}^{\mathrm{Si}}_{\mathrm{NBO}}\}\approx\{1, 2\}$ for S46 and $\{\overline{N}^{\mathrm{B}}_{\mathrm{NBO}}, \overline{N}^{\mathrm{Si}}_{\mathrm{NBO}}\}\approx\{0.75, 1.5\}$ for S49. For the S46 glass members, this implies roughly two and one NBO species per SiO_4 and BO_3 group, respectively. In contrast, the more polymerized S49 networks involve SiO_4 tetrahedra that on the average coordinate ≈1.5 NBO (consistent with similar Q^2_{Si} and Q^3_{Si} populations; see Fig. **2**), while ≈25% of the $\{BO_3\}$ ensemble is devoid of NBO species.

Given that the S46 glass networks involve an NBO distribution peaked around ≈1 NBO per BO_3 moiety, whereas those of the S49 structures comprise BO_3 groups that accommodate either 0 or 1 NBO, one may ask if our ^{11}B NMR data of Figs. **3** and **6** may resolve these resonances. The shift-spans compiled in Fig. **6**(k) from literature data[51,55,56,72–79] (relevant for the peak maxima along the isotropic projection of 3QMAS spectra) suggest an overall minor deshielding of the $^{11}BO_3$ environments for an increasing number of NBO anions, but also manifests strongly overlapping shift ranges from $^{11}BO_3$ moieties with 0 and 1 NBO ions. Hence, these resonances cannot be separated with the 3QMAS NMR spectra resolution offered from our glasses. Nevertheless, significant contributions from $^{11}BO_3$ groups with two or three NBO species may be excluded [Fig. **6**(k)], in full accordance with our estimates above and further corroborated by the "typical" isotropic chemical-shift ranges displayed in Fig. **6**(l) that are relevant for the ^{11}B MAS NMR spectra of the right panel of Fig. **6**.

5.3 BPS Structural Model

5.3.1 Glass Building Blocks and Bond Preferences

Here we summarize our results for the various phosphate, silicate, and borate building blocks and discuss their (expected) preferences for interlinking in the BPS glass structure. For both S46/S49 BPS families, the phosphate ensemble constitutes a main component of isolated orthophosphate (Q^0_P) tetrahedra (86–96%) that in direct analogy of the B-free silicate glasses[35] assume interstitial positions around the borosilicate network. The remaining portion (Q^1_P) form predominantly P–O–**Si** bonds (as opposed to P–O–**B**; to be discussed elsewhere), where they terminate segments of the (boro)silicate network. In the BPS glasses, B mainly exists as planar BO_3 groups that constitute 66–83% and 57–64% of the total B speciation in the S46 and S49 glass series, respectively, with BO_4 species accounting for the remaining. The $x^{[4]}_B$ population increases concomitantly with the B_2O_3 content.

The networks of the parent B-free $S46_{2.6}(0)$ and $S49_{4.0}(0)$ glasses comprise mainly interconnected Q^2_{Si} and $\{Q^2_{Si}, Q^3_{Si}\}$ silicate groups, respectively (see Fig. **2**). A slight increase in $\overline{N}^{Si}_{BO}$ by up to ≈0.2 results when B is introduced, because some NBO ions relocate to the BO_3 groups, which on the average accommodate ≈1 and ≈0.7–0.8 NBO species in the B-bearing S46 and S49 glasses, respectively. Yet, the $\{Q^n_{Si}\}$ speciation is expected to remain overall intact, except that Si–O–**Si** bonds are gradually replaced by Si–O–$\mathbf{B}^{[4]}$ (major) and Si–O–$\mathbf{B}^{[3]}$ (minor) linkages in the borosilicate network. The tetrahedral SiO_4 and BO_4 species strongly prefer to interconnect. This implies that $B^{[4]}$(4Si) groups solely involving bonds to Si account for >70% of all BO_4 units in the Si-richest $S49_{4.0}(2)$, $S49_{4.0}(5)$, and $S46_{2.6}(5)$ glasses; see Fig. **7**. The average number of bonds to Si remains $\gtrsim 3$ until ≈40% of the SiO_2 reservoir is replaced by B_2O_3. Yet, a relatively high mean number $\overline{N}_{Si} \approx 2.7$ of $B^{[4]}$–O–Si bonds persists even in the B-richest $S46_{2.6}(37)$ structure. The estimated preference factor $P_{Si} \approx 0.5$ is equivalent to a scenario with two Si neighbors around each

BO_4 tetrahedron, while the remaining two positions are filled statistically by Si and $B^{[3]}$ atoms according to their relative abundances in the glass. The $B^{[3]}$ coordinations prefer connecting to other species according to $B^{[3]}$ >$B^{[4]}$ >Si. Hence, despite that the total number of $B^{[3]}$–O–$B^{[4]}$ bonds increases concurrently with the B_2O_3 content at the expense of the $B^{[3]}$(1Si) [*i.e.* "non-ring"] fraction, the $B^{[3]}$(0Si) ["ring"] groups mainly associate with themselves as boroxol rings, regardless of the precise x_B/x_{Si} ratio and total NBO content of the BPS structure.

5.3.2 Medium-Range Structural Organization

The pronounced propensities for $B^{[3]}$–O–$B^{[3]}$ and $B^{[4]}$–O–Si bond formation imply that the BPS glass structure likely comprises (sub)nm-sized "domains" of borosilicate (involving Si–O–Si and Si–O–$B^{[4]}$ bonds) and borate ($B^{[3]}$–O–$B^{[3]}$ fragments in boroxol rings) networks, similar to the organization of the Pyrex® structure discussed in refs.[80–82] These borate/borosilicate networks are connected through $B^{[3]}$–O–**B**$^{[4]}$–O–Si and $B^{[3]}$–O–Si fragments, with the former constellation generally prevailing. Some of these moieties likely also participate in "superstructural" borate units.[38,54,74,79,81] The "direct" contact points between the BO_3 and SiO_4 groups, *i.e.*, the $B^{[3]}$(1Si) ("non-ring") moieties, are only abundant in the Si-rich glasses and they are gradually replaced by $B^{[3]}$(0Si) species when the B content of the glass is increased (see Table **3**).

The relative proportions of these borate/borosilicate domains depends on the x_B/x_{Si} ratio of the glass. For instance, the Si-rich $S46_{2.6}(5)$ structure associated with x_B/x_{Si}=0.22 and $x_B^{[4]}$=0.17 (see Tables **1** and **3**) is dominated by a silicate network of Q^2_{Si} groups cross-linked by $B^{[4]}$(4Si) species. This Si-rich borosilicate network co-exist with a domain of boroxol rings featuring ≈1 NBO per BO_3 moiety. The two networks are merged by $B^{[4]}$(3Si) and $B^{[3]}$(1Si) groups. When the B_2O_3 content is increased, the number of BO_4 groups increases in the borosilicate network, while $B^{[4]}$(3Si), $B^{[4]}$(2Si)—and to a lesser extent $B^{[3]}$(1Si)—species constitute bridges to the boroxol

rings. The B-richest $S46_{2.6}(37)$ structure comprises mainly boroxol rings that are cross-linked by $B^{[4]}(3Si)$ and $B^{[4]}(2Si)$ groups to a borosilicate network dominated by BO_4 groups; the latter is overall more condensed than those of the Si-rich S46 glasses, due to the absence of NBO species at the BO_4 tetrahedra and because the Q^2_{Si} groups are minor components (x_B/x_{Si}=8.00). Since the BO_3 groups now grossly outnumber the SiO_4 tetrahedra, most of the NBO reservoir resides at the boroxol rings (section **5.2**).

5.4 Implications for Glass Dissolution

Here we discuss our structural model in conjunction with general glass degradation trends reported in the literature for borosilicate/BPS glasses. We identify two structural descriptors that we expect to primarily control the dissolution rate of BPS glasses in aqueous solutions, and highlight some remaining structural questions that must be addressed for achieving bioactive BPS glasses with tailored solubility in (simulated) body fluids.

On their immersion in aqueous solutions, borate-based BGs are claimed to (**A**) degrade faster and (**B**) convert more completely to HCA relative to their silicate-based counterparts.[4–6,11,12] However, few (if any) *direct* experimental comparisons of the HCA formation among borate-bearing/free BGs are reported. The hitherto lacking detailed structural understanding of BPS glasses hampers a rational design for tuning the glass degradability ("solubility") in aqueous media.

Concerning (**B**), it remains unclear if the HCA formation *rate* or *amount* thereof formed are obviously higher than those observed from highly bioactive silicate-based BGs such as the "45S5" composition,[15] *i.e.*, $S46_{2.6}(0)$. As commented by Lepry and Nazhat,[14] essentially all *in vitro* evaluations of HCA formation from B-bearing BGs employed solutions with 20–250 times higher phosphate concentrations than human plasma or its acellular *simulated body fluid* (SBF)[83] counterpart that has become the standard medium for *in vitro* testing. For a melt-prepared B-based 45S5

composition[4,5] ($S46_{2.6}(46)$ in our notation), an induction time of 3 days for HCA formation in SBF was reported,[14] which is significantly longer than that $\lesssim$12 h[84] observed for the original 45S5 formulation. More direct *in vitro* comparisons between silicate/borate-based BGs in SBF are required to evaluate their relative merits for HCA formation.

We next consider the glass degradability in aqueous media, *i.e.*, (**A**). For (phospho)silicate glasses, it is well-known that a decrease in the silicate network connectivity ($\overline{N}_{\mathrm{BO}}^{\mathrm{Si}}$) accelerates the glass dissolution.[20,23,42] Solubility data are not gathered for our BPS glasses, but one expects from the more condensed $S49_{4.0}(0)$ network ($\overline{N}_{\mathrm{BO}}^{\mathrm{Si}} = 2.54$) that it degrades slower than its $S46_{2.6}(0)$ counterpart ($\overline{N}_{\mathrm{BO}}^{\mathrm{Si}} = 2.11$). The literature inarguably shows that the incorporation of B into a silicate-based glass increases its dissolution in aqueous media,[19,20] as well as that bioactive BPS glasses dissolve more rapidly than their B-free counterparts.[4–9] However, that same literature on BG applications is vague regarding the underlying reasons: by assuming that B is exclusively present as BO_3 groups in the glass structure, Yao *et al.* attributed the comparatively faster degradation of borate/borosilicate glasses to the lower connectivity of the $B^{[3]}$ coordinations relative to $Si^{[4]}$.[5] Yet, the silicate network connectivity of *bioactive* silicate-based glasses remains $\overline{N}_{\mathrm{BO}}^{\mathrm{Si}} < 3$ (refs.[23,41,42]) and is consequently *lower* than that of vitreous B_2O_3. Moreover, as shown herein, the networks of Na/Ca-modified BPS glasses also comprise fully polymerized—and thereby highly cross-linking—BO_4 tetrahedra. The higher degradability of B-bearing phosphosilicate glasses merely stems from the higher hydrolysis rate of B–O bonds relative to Si–O, with the *reactivity increasing* in the order[19,20]

$$\mathrm{Si–O–Si} < \mathrm{Si–O–B^{[4]}} < \mathrm{B^{[3]}–O–B^{[3]}}. \tag{8}$$

This reactivity order coupled with the progressive replacements of Si–O–Si by Si–O–B and (particularly) B–O–B bonds rationalize the elevated glass dissolution observed[4,5] when B replaces Si in the (boro)silicate networks. Moreover, the combined effects from the higher cross-linking

of $B^{[4]}$ coordinations and a slower hydrolysis of the $B^{[4]}$–O–Si bonds relative to the $B^{[3]}$–O–$B^{[3]}$ linkages[19,20] make the *borosilicate* network portions of the BPS glass more durable. At a constant cation composition and total NBO content, it follows that the higher the $x_B^{[4]}$ fraction in the BG structure, the more resistant to aqueous attack the glass structure becomes. Hence, the parameter-pair $\{\overline{N}_{BO}^{Si}, x_B^{[4]}\}$ should primarily govern the solubility of BPS glasses, where the following trends are predicted for the S46/S49 members: (*i*) At a fixed x_B/x_{Si} ratio, the lower $\{\overline{N}_{BO}^{Si}, x_B^{[4]}\}$ values of an S46-based glass implies a faster degradation than its S49 analog. (*ii*) However, relative to the S46 networks, the S49-based counterparts should exhibit *less variations* in solubility for increasing B_2O_3 substitution degree, since the *alteration* of the $B^{[4]}$ fraction is *smaller* among the S49 members (see Table **3**). We note that all arguments above draw from well-established dissolution trends of (P-free) borate/borosilicate glasses,[19,20] which become applicable to the present BPS glasses with low P contents thanks to the herein established BPS structural model of borate/borosilicate networks surrounded by orthophosphate ions (see sections **4.1** and **5.3.1**). Hence, when ignoring the small Q_P^1 population, any given BPS glass network is an approximation of a borosilicate counterpart, as argued in section **2.2**.

Noteworthy, $x_B^{[4]}$ increases concurrently with $x(SiO_2)$ at constant modifier content in the glass; see Table **3**. Hence, lowering the SiO_2 content improves the solubility because *both* the numbers of Si–O–Si bonds and network-condensing BO_4 moieties are reduced. The YDBX model[37,38] predicts that a further increase in the total Na^+/Ca^{2+} content of these *modifier-rich* bioactive BPS glasses drives $B^{[4]} \rightarrow B^{[3]}$ conversions at a constant x_B/x_{Si} ratio. Consequently, increasing the modifier content of a borosilicate/BPS glass will accelerate its degradability because either/both of the $\{\overline{N}_{BO}^{Si}, x_B^{[4]}\}$ parameters is/are decreased. Future work will need to settle which structural role the surplus modifiers predominantly assumes—as charge compensators of BO_4 groups or of NBO ions? Such insight combined with the herein reported near invariance of the silicate network polymerization

when Si is replaced by B at a constant modifier content (section **4.2**) should allow for tuning each $\{\overline{N}_{\mathrm{BO}}^{\mathrm{Si}}, x_{\mathrm{B}}^{[4]}\}$ parameter almost independently for a given $\{x_{\mathrm{B}}, x_{\mathrm{Si}}, x_{\mathrm{P}}\}$ glass composition. We stress that our proposed role of $\{\overline{N}_{\mathrm{BO}}^{\mathrm{Si}}, x_{\mathrm{B}}^{[4]}\}$ to (primarily) govern the BPS glass dissolution is *independent* on *how* these values were arranged; while $\overline{N}_{\mathrm{BO}}^{\mathrm{Si}}$ and $x_{\mathrm{B}}^{[4]}$ depend foremost on the BPS glass composition, particularly the B speciation may display a weak dependence on the thermal history of the glass.

6 Conclusions

We have proposed a structural model for modifier-rich Na_2O–CaO–B_2O_3–SiO_2–P_2O_5 glasses with relatively low P contents [$x(P_2O_5)\leqslant 0.04$] and variable $x(SiO_2)/x(B_2O_3)$ ratios. The following structural alterations are observed when SiO_2 is gradually replaced by B_2O_3 at a constant glass-modifier content:

(*i*) The phosphate speciation and the average silicate network polymerization only change marginally, where the minor increase of the Q_{P}^1 population (reflecting the extents of Si–O–P bonding) stems from the concurrent silicate-network condensation.[33] Both these trends originate from (*ii*) a redistribution of NBO species from the SiO_4 tetrahedra to the BO_3 groups, which on the average accommodate 0.7–1 NBO ions per B atom. (*iii*) Notwithstanding that $B^{[3]}$ coordinations dominate the B speciation throughout all glasses, a progressive $B^{[3]} \rightarrow B^{[4]}$ conversion is observed for increasing $x(B_2O_3)$. Yet, regardless of the B_2O_3 content, the more condensed and Si-rich S49 glass networks manifest consistently higher fractional populations of BO_4 tetrahedra (37–43%) than their S46 counterparts (17–34%). The $x_{\mathrm{B}}^{[4]}$ fraction in the S49 glasses reaches a plateau at ≈43% already when 30% of the SiO_2 reservoir is replaced by B_2O_3, whereas minor transformations from trigonal to tetrahedral B coordinations are observed throughout the entire range of B-for-Si substitutions in the S46 series.

The medium-range BPS glass structure is mainly governed by the strong preferences for $B^{[3]}$–O–$B^{[3]}$ and $B^{[4]}$–O–Si bonding scenarios relative to other options, such as $B^{[3]}$–O–$B^{[4]}$ and $B^{[3]}$–O–Si. Along previous reports on borosilicate glasses of low modifier content,[50–52] substantial amounts of $B^{[3]}$–O–Si contacts are only observed in Si-rich BPS networks, whereas they are sparse in structures exhibiting comparable amounts of B and Si. From these bonding preferences, we inferred a BPS structural model that comprises (sub)nm-sized "domains" of a borate network (BO_3 groups in boroxol rings) interlinked with a borosilicate network through $B^{[4]}$(3Si), $B^{[4]}$(2Si), and $B^{[3]}$(1Si) moieties.

We proposed that the parameter-pair $\{\overline{N}^{\mathrm{Si}}_{\mathrm{BO}},\ x^{[4]}_{\mathrm{B}}\}$ primarily dictates the solubility of alkali/alkaline-earth bearing BPS glasses, whose degradation should *decrease* concurrently with an *increase* in either the silicate network polymerization or the $B^{[4]}$ population. The improved insight about the alterations of these parameters when Si is replaced by B gained from our study should allow for tailoring the glass solubility in (simulated) body fluids. Moreover, for biomedical applications, a high amount of readily leached orthophosphate ions is believed to improve the HCA formation.[23,33,36] We are currently exploring the glass-formation limits of P-richer BPS glasses to verify that the beneficial structural feature of a PO_4^{3-}-dominated phosphate speciation remains also in this composition regime, as well as for locating the permissible range of $x(SiO_2)/x(B_2O_3)$ and $x(Na_2O)/x(CaO)$ molar ratios that yield homogeneous glasses. Further work is required to verify the overall validity of the herein proposed borate/borosilicate BPS network organization, which was conjectured from standard ^{29}Si, ^{31}P, and ^{11}B (3Q)MAS NMR experimentation. Hence, our future investigations will merely target a more direct probing of the medium-range glass structure by utilizing advanced homo/heteronuclear NMR techniques.[3,85]

Acknowledgements

This work was supported by the Swedish Research Council (contract VR-NT 2014-4667). We thank Baltzar Stevensson for help, and Di Zhang and Renny Mathew for glass synthesis input at an early stage of this project. We also thank R. M. for recording the ^{29}Si NMR spectrum from the $S49_{4.0}(0)$ glass.

References

1 G. Engelhardt and D. Michel, *High-Resolution Solid-State NMR Spectroscopy of Silicates and Zeolites*, Wiley, Chicester, 1987.

2 G. N. Greaves and S. Sen, *Adv. Phys.*, 2007, **56**, 1–166.

3 M. Edén, *Annu. Rep. Prog. Chem., Sect. C: Phys. Chem.*, 2012, **108**, 177–221.

4 W. Huang, D. E. Day, K. Kittiratanapiboon, and M. N. Rahaman, *J. Mater. Sci. Mater. Med.*, 2006, **17**, 583–596.

5 A. Yao, D. Wang, W. Huang, Q. Fu, M. N. Rahaman, and D. E. Day, *J. Am. Ceram. Soc.*, 2007, **90**, 303–306.

6 R. F. Brown, M. N. Rahaman, A. B. Dwilewicz, W. Huang, D. E. Day, Y. Li, and B. S. Bal, *J. Biomed. Mater. Res.*, 2009, **88A**, 392–400.

7 X. Liu, W. Huang, H. Fu, A. Yao, D. Wang, H. Pan, W. W. Lu, X. Jiang, and X. Zhang, *J. Mater. Sci. Mater. Med.*, 2009, **20**, 1237–1243.

8 H. B. Pan, X. L. Zhao, X. Zhang, K. B. Zhang, L. C. Li, Z. Y. Li, W. M. Lam, W. W. Lu, D. P. Wang, W. H. Huang, K. L. Lin, and J. Chang, *J. R. Soc. Interface*, 2010, **7**, 1025–1031.

9 M. N. Rahaman, D. E. Day, B. S. Bal, Q. Fu, S. B. Jung, L. F. Bonewald, and A. P. Tomsia, *Acta Biomater.*, 2011, **7**, 2355–2373.

10 X. Yang, L. Zhang, X. Chen, X. Sun, G. Yang, X. Guo, H. Yang, C. Gao, and Z. Gou, *J. Non-Cryst. Solids*, 2012, **358**, 1171–1179.

11 Q. Fu, M. N. Rahaman, and D. E. Day, *J. Am. Ceram. Soc.*, 2009, **92**, 1551–2916.

12 X. Liu, M. N. Rahaman, and D. E. Day, *J. Mater. Sci. Mater. Med.*, 2013, **24**, 583–595.

13 L. A. Haro Durand, G. E. Vargas, N. M. Romero, R. Vera-Mesones, J. M. Porto-López, A. R. Boccaccini, M. P. Zago, A. Baldi, and A. Gorustovich, *J. Mater. Chem. B*, 2015, **3**, 1142–1148.

14 W. C. Lepry and S. N. Nazhat, *Chem. Mater.*, 2015, **27**, 4821–4831.

15 L. L. Hench, *J. Am. Ceram. Soc.*, 1991, **74**, 1487–1510.

16 L. L. Hench and J. M. Polak, *Science*, 2002, **295**, 1014–1017.

17 J. R. Jones, *Acta Biomater.*, 2013, **9**, 4457–4486.

18 M. Brink, T. Turunen, R.-P. Happonen, and A. Yli-Urpo, *J. Mater. Sci: Mater. Med.*, 1997, **37**, 114–121.

19 B. C. Bunker, G. W. Arnold, D. E. Day, and P. J. Bray, *J. Non-Cryst. Solids*, 1986, **87**, 226–253.

20 B. C. Bunker and W. H. Casey, *The Aqueous Chemistry of Oxides*, Oxford University Press, Oxford, 2016.

21 A. Hoppe, N. S. Güldal, and A. R. Boccaccini, *Biomaterials*, 2012, **32**, 2757–2774.

22 M. D. O'Donnell, S. J. Watts, R. V. Law, and R. G. Hill, *J. Non-Cryst. Solids*, 2008, **354**, 3554–3560.

23 M. Edén, *J. Non-Cryst. Solids*, 2011, **357**, 1595–1602.

24 H. Gan, P. C. Hess, and R. J. Kirkpatrick, *Geochim. Cosmochim. Acta*, 1994, **58**, 4633–4647.

25 H. Yamashita, K. Nagata, H. Yoshino, K. Ono, and T. Maekawa, *J. Non-Cryst. Solids*, 1999, **248**, 115–126.

26 F. Muñoz, L. Montagne, L. Delevoye, A. Durán, L. Pascual, S. Cristol, and J.-F. Paul, *J. Non-Cryst. Solids*, 2006, **352**, 28–29.

27 M. Sitarz, K. Bulat, and Z. Olejniczak, *Vib. Spectrosc.*, 2012, **61**, 72–77.

28 R. Dupree, D. Holland, M. G. Mortuza, J. A. Collins, and M. W. G. Lockyer, *J. Non-Cryst. Solids*, 1988, **106**, 403–407.

29 M. W. G. Lockyer, D. Holland, and R. Dupree, *Phys. Chem. Glasses*, 1995, **36**, 22–30.

30 M. W. G. Lockyer, D. Holland, and R. Dupree, *J. Non-Cryst. Solids*, 1995, **188**, 207–219.

31 V. FitzGerald, D. M. Pickup, D. Greenspan, G. Sarkar, J. J. Fitzgerald, K. M. Wetherall, R. M. Moss, J. R. Jones, and R. J. Newport, *Adv. Funct. Mater.*, 2007, **17**, 3746–3753.

32 R. Mathew, C. Turdean-Ionescu, B. Stevensson, I. Izquierdo-Barba, A. García, D. Arcos, M. Vallet-Regí, and M. Edén, *Chem. Mater.*, 2013, **25**, 1877–1885.

33 R. Mathew, B. Stevensson, A. Tilocca, and M. Edén, *J. Phys. Chem. B*, 2014, **118**, 833–844.

34 R. Mathew, B. Stevensson, and M. Edén, *J. Phys. Chem. B*, 2015, **119**, 5701–5715.

35 B. Stevensson, R. Mathew, and M. Edén, *J. Phys. Chem. B*, 2014, **118**, 8863–8876.

36 A. Tilocca and A. N. Cormack, *J. Phys. Chem. B*, 2007, **111**, 14256–14264.

37 Y. H. Yun and P. J. Bray, *J. Non-Cryst. Solids*, 1978, **27**, 363–380.

38 W. J. Dell, P. J. Bray, and S. Z. Xiao, *J. Non-Cryst. Solids*, 1983, **58**, 1–16.

39 B. C. Bunker, D. R. Tallant, R. J. Kirkpatrick, and G. L. Turner, *Phys. Chem. Glasses*, 1990, **31**, 30–41.

40 M. Edén, P. Sundberg, and C. Stålhandske, *J. Non-Cryst. Solids*, 2011, **357**, 1587–1594.

41 Z. Strnad, *Biomaterials*, 1992, **13**, 317–321.

42 R. Hill, *J. Mater. Sci. Lett.*, 1996, **15**, 1122–1125.

43 K. L. Geisinger, R. Oestrike, A. Navrotsky, G. L. Turner, and R. J. Kirkpatrick, *Geochim. Cosmochim. Acta*, 1988, **52**, 2405–2414.

44 A. D. Irwin, J. S. Holmgren, and J. Jonas, *J. Non-Cryst. Solids*, 1988, **101**, 249–254.

45 S. W. Martin, D. Bain, K. Budhwani, and S. Feller, *J. Am. Ceram. Soc.*, 1992, **75**, 1117–1122.

46 G. El-Damrawi and W. Müller-Warmuth, *J. Non-Cryst. Solids*, 1992, **146**, 137–144.

47 L. van Wüllen, W. Müller-Warmuth, D. Papageorgiou, and H. J. Pentinghaus, *J. Non-Cryst. Solids*, 1994, **171**, 53–67.

48 S. Wang and J. F. Stebbins, *J. Am. Ceram. Soc.*, 1999, **82**, 1519–1528.

49 R. Martens and W. Müller-Warmuth, *J. Non-Cryst. Solids*, 2000, **265**, 167–175.

50 L.-S. Du and J. F. Stebbins, *J. Non-Cryst. Solids*, 2003, **315**, 239–255.

51 L.-S. Du and J. F. Stebbins, *J. Phys. Chem. B*, 2003, **107**, 10063–10076.

52 L.-S. Du and J. F. Stebbins, *Chem. Mater.*, 2003, **15**, 3913–3921.

53 M. M. Smedskjaer, J. C. Mauro, R. E. Youngman, C. L. Hogue, M. Potuzak, and Y. Yue, *J. Phys. Chem. B*, 2011, **115**, 12930–12946.

54 D. Möncke, G. Tricot, A. Winterstein-Beckmann, L. Wondraczek, and E. I. Kamitsos, *Phys. Chem. Glasses: Eur. J. Glass Sci. Technol., Part B*, 2015, **56**, 203–211.

55 R. E. Youngman and J. W. Zwanziger, *J. Non-Cryst. Solids*, 1994, **168**, 293–297.

56 F. Angeli, T. Charpentier, D. De Ligny, and C. Cailleteau, *J. Am. Ceram. Soc.*, 2010, **93**, 2693–2704.

57 L. Frydman and J. S. Harwood, *J. Am. Chem. Soc.*, 1995, **117**, 5367–5368.

58 J.-P. Amoureux, C. Fernandez, and S. Steurnagel, *J. Magn. Reson. Ser. A*, 1996, **123**, 116–118.

59 T. Vosegaard, P. Florian, P. J. Grandinetti, and D. Massiot, *J. Magn. Reson.*, 2000, **143**, 217–222.

60 P. K. Madhu, A. Goldbourt, L. Frydman, and S. Vega, *Chem. Phys. Lett.*, 1999, **307**, 41–47.

61 D. J. States, R. A. Haberkorn, and D. J. Ruben, *J. Magn. Reson.*, 1982, **48**, 286–292.

62 Y. Millot and P. P. Man, *Solid State Nucl. Magn. Reson.*, 2002, **21**, 21–43.

63 H. Grussaute, L. Montagne, G. Palavit, and J. L. Bernard, *J. Non-Cryst. Solids*, 2000, **263**, 312–317.

64 E. Leonova, I. Izquierdo-Barba, D. Arcos, A. López-Noriega, N. Hedin, M. Vallet-Regí, and M. Edén, *J. Phys. Chem. C*, 2008, **112**, 5552–5562.

65 F. Fayon, C. Duée, T. Poumeyrol, M. Allix, and D. Massiot, *J. Phys. Chem. C*, 2013, **117**, 2283–2288.

66 A.-R. Grimmer, M. Mägi, M. Hähnert, H. Stade, A. Samoson, W. Weiker, and E. Lippmaa, *Phys. Chem. Glasses*, 1984, **25**, 105–109.

67 H. Maekawa, T. Maekawa, K. Kawamura, and T. Yokokawa, *J. Non-Cryst. Solids*, 1991, **127**, 53–64.

68 D. Massiot, C. Bessada, J. P. Coutures, and F. Taulelle, *J. Magn. Reson.*, 1990, **90**, 231–242.

69 L. van Wüllen and W. Müller-Warmuth, *Solid State Nucl. Magn. Reson.*, 1993, **2**, 279–284.

70 P. R. Bodart, *J. Magn. Reson.*, 1998, **133**, 207–209.

71 S. Wegner, L. van Wüllen, and G. Tricot, *Solid State Sciences*, 2010, **12**, 428–439.

72 J. F. Stebbins, P. Zhao, and S. Kroeker, *Solid State Nucl. Magn. Reson.*, 2000, **16**, 9–19.

73 S. Kroeker and J. F. Stebbins, *Inorg. Chem.*, 2001, **40**, 6239–6246.

74 P. M. Aguiar and S. Kroeker, *Solid State Nucl. Magn. Reson.*, 2005, **27**, 10–15.

75 P. M. Aguiar and S. Kroeker, *J. Non-Cryst. Solids*, 2007, **353**, 1834–1839.

76 M. R. Hansen, T. Vosegaard, H. J. Jakobsen, and J. Skibsted, *J. Phys. Chem. A*, 2004, **108**, 586–594.

77 J. Banerjee, G. Ongie, J. Harder, T. Edwards, C. Larson, S. Sutton, A. Moeller, A. Basu, M. Affatigato, S. Feller, M. Kodama, P. M. Aguiar, and S. Kroeker, *J. Non-Cryst. Solids*, 2006, **352**, 674–678.

78 D. Holland, S. A. Feller, T. F. Kemp, M. E. Smith, A. P. Howes, D. Winslow, and M. Kodama, *Phys. Chem. Glasses: Eur. J. Glass Sci. Technol., Part B*, 2007, **48**, 1–8.

79 O. L. G. Alderman, D. Iuga, A. P. Howes, K. J. Pike, D. Holland, and R. Dupree, *Phys. Chem. Chem. Phys.*, 2013, **15**, 8208–8221.

80 J. C. Phillips and R. Kerner, *J. Chem. Phys.*, 2008, **128**, 174506.

81 A. P. Howes, N. M. Vedishcheva, A. Samoson, J. V. Hanna, M. E. Smith, D. Holland, and R. Dupree, *Phys. Chem. Chem. Phys.*, 2011, **13**, 11919–11928.

82 M. M. Smedskjaer, R. E. Youngman, and J. C. Mauro, *Appl. Phys. A*, 2014, **116**, 491–504.

83 T. Kokubo, H. Kushitani, S. Sakka, T. Kitsugi, and T. Yamamuro, *J. Biomed. Mater. Res.*, 1990, **24**, 721–734.

84 I. Lebecq, F. Désanglois, A. Leriche, and C. Follet-Houttemane, *J. Biomed. Mater. Res.*, 2007, **83A**, 156–168.

85 M. Edén, *Solid State Nucl. Magn. Reson.*, 2009, **36**, 1–10.

Table 1: Glass Compositions[a]

label	f/% [b]	$x(Na_2O)$	$x(CaO)$	$x(SiO_2)$	$x(B_2O_3)$	$x(P_2O_5)$	stoichiometric formula[c]	x_{Na}/x_{Ca} [d]	x_B/x_{Si} [d]	R' [e]	K [f]
$S46_{2.6}(0)$	0	0.246	0.267	0.461	0.000	0.026	$Na_{0.173}Ca_{0.094}Si_{0.162}B_{0.000}P_{0.018}O_{0.552}$	1.84	0.00	–	–
$S46_{2.6}(5)$	10	0.246	0.267	0.415	0.046	0.026	$Na_{0.168}Ca_{0.091}Si_{0.142}B_{0.031}P_{0.018}O_{0.550}$	1.84	0.22	9.46	9.00
$S46_{2.6}(9)$	20	0.246	0.267	0.369	0.092	0.026	$Na_{0.163}Ca_{0.088}Si_{0.122}B_{0.061}P_{0.017}O_{0.548}$	1.84	0.50	4.73	4.00
$S46_{2.6}(14)$	30	0.246	0.267	0.322	0.138	0.026	$Na_{0.158}Ca_{0.086}Si_{0.104}B_{0.089}P_{0.017}O_{0.547}$	1.84	0.86	3.15	2.33
$S46_{2.6}(18)$	40	0.246	0.267	0.277	0.184	0.026	$Na_{0.153}Ca_{0.083}Si_{0.086}B_{0.115}P_{0.016}O_{0.546}$	1.84	1.33	2.37	1.50
$S46_{2.6}(28)$	60	0.246	0.267	0.184	0.277	0.026	$Na_{0.145}Ca_{0.079}Si_{0.054}B_{0.163}P_{0.015}O_{0.543}$	1.84	3.00	1.58	0.67
$S46_{2.6}(37)$	80	0.246	0.267	0.092	0.369	0.026	$Na_{0.138}Ca_{0.075}Si_{0.026}B_{0.206}P_{0.015}O_{0.541}$	1.84	8.00	1.18	0.25
$S49_{4.0}(0)$	0	0.241	0.233	0.486	0.000	0.040	$Na_{0.165}Ca_{0.079}Si_{0.166}B_{0.000}P_{0.027}O_{0.562}$	2.08	0.00	–	–
$S49_{4.0}(2)$	5	0.241	0.233	0.462	0.024	0.040	$Na_{0.162}Ca_{0.078}Si_{0.155}B_{0.016}P_{0.027}O_{0.561}$	2.08	0.11	14.7	19.0
$S49_{4.0}(5)$	10	0.241	0.233	0.437	0.049	0.040	$Na_{0.160}Ca_{0.077}Si_{0.145}B_{0.032}P_{0.026}O_{0.560}$	2.08	0.22	7.37	9.00
$S49_{4.0}(7)$	15	0.241	0.233	0.413	0.073	0.040	$Na_{0.157}Ca_{0.076}Si_{0.134}B_{0.047}P_{0.026}O_{0.559}$	2.08	0.35	4.91	5.67
$S49_{4.0}(10)$	20	0.241	0.233	0.389	0.097	0.040	$Na_{0.155}Ca_{0.075}Si_{0.125}B_{0.062}P_{0.026}O_{0.558}$	2.08	0.50	3.69	4.00
$S49_{4.0}(15)$	30	0.241	0.233	0.340	0.146	0.040	$Na_{0.150}Ca_{0.072}Si_{0.106}B_{0.091}P_{0.025}O_{0.557}$	2.08	0.86	2.46	2.33
$S49_{4.0}(19)$	40	0.241	0.233	0.292	0.194	0.040	$Na_{0.146}Ca_{0.070}Si_{0.088}B_{0.117}P_{0.024}O_{0.555}$	2.08	1.33	1.85	1.50
$S49_{4.0}(24)$	50	0.241	0.233	0.243	0.243	0.040	$Na_{0.141}Ca_{0.068}Si_{0.071}B_{0.142}P_{0.023}O_{0.553}$	2.08	2.00	1.48	1.00

[a]Each glass is labeled $SN_p(q)$, where $N = 100[x(SiO_2) + x(B_2O_3)]$ is the sum of mol% of SiO_2 and B_2O_3, whereas p and q are the mol% of P_2O_5 and B_2O_3, respectively.

[b]$f = 100x(B_2O_3)/[x(SiO_2) + x(B_2O_3)]$ is the percentage of B_2O_3 substitution for SiO_2.

[c]Stoichiometric formula with coefficients specified as atom fractions that sum to unity.

[d]Ratios of the atomic fractions of Na and Ca (x_{Na}/x_{Ca}), and B and Si (x_B/x_{Si}), respectively.

[e]Ratio $R' = x(\mathcal{M}_2O)/x(B_2O_3) = x_{\mathcal{M}}/x_B$, with $x_{\mathcal{M}}$ calculated from eq. (1).

[f]$K = x(SiO_2)/x(B_2O_3)$.

Table 2: ^{31}P and ^{29}Si NMR Results

	^{31}P NMR Data[a]								^{29}Si NMR Data[b]		
label	δ^{P}_{max} (ppm)	W_P (ppm)	δ^{0}_{P} (ppm)	W^{0}_{P} (ppm)	x^{0}_{P}	δ^{1}_{P} (ppm)	W^{1}_{P} (ppm)	x^{1}_{P}	δ^{Si}_{max} (ppm)	δ^{Si}_{CG} (ppm)	W_{Si} (ppm)
$S46_{2.6}(0)$	8.72	7.50	8.7	7.4	0.959	0.4	7.3	0.041	−79.5	−81.0	11.1
$S46_{2.6}(5)$	8.60	7.35	8.6	7.2	0.952	0.4	7.1	0.048	−80.0	−80.7	11.9
$S46_{2.6}(9)$	8.46	7.37	8.5	7.2	0.952	0.4	7.1	0.048			
$S46_{2.6}(14)$	8.35	7.41	8.4	7.3	0.952	0.4	6.8	0.048	−79.9	−80.5	12.4
$S46_{2.6}(18)$	8.27	7.44	8.3	7.3	0.949	0.4	6.8	0.051			
$S46_{2.6}(28)$	8.07	7.53	8.1	7.4	0.941	0.4	6.8	0.059	−79.5	−80.1	12.7
$S46_{2.6}(37)$	7.79	7.57	7.8	7.4	0.935	0.4	6.6	0.065	−78.6	−79.6	12.5
$S49_{4.0}(0)$	8.34	7.46	8.3	7.3	0.900	0.0	7.8	0.100	−82.5	−84.9	16.0
$S49_{4.0}(2)$	8.28	7.49	8.3	7.3	0.897	0.0	7.8	0.103	−82.8	−84.4	15.7
$S49_{4.0}(5)$	8.14	7.52	8.1	7.3	0.897	0.0	7.6	0.103			
$S49_{4.0}(7)$	8.08	7.55	8.1	7.3	0.893	0.0	7.6	0.107	−83.2	−84.2	15.0
$S49_{4.0}(10)$	7.96	7.59	8.0	7.4	0.890	0.0	7.5	0.110			
$S49_{4.0}(15)$	7.97	7.66	7.9	7.4	0.887	0.0	7.2	0.113			
$S49_{4.0}(19)$	7.64	7.76	7.6	7.5	0.871	0.0	7.3	0.129			
$S49_{4.0}(24)$	7.51	7.85	7.5	7.5	0.864	0.0	7.3	0.136	−82.9	−84.0	14.3

[a]Shift at peak maximum (δ^{P}_{max}; uncertainty ±0.08 ppm) and full width at half maximum (fwhm) height (W_P; ±0.15 ppm) of the net ^{31}P NMR signal, as well as the chemical shift (δ^{n}_{P}; ±0.3 ppm), fwhm height (W^{n}_{P}; ±0.5 ppm), and fractional population (x^{n}_{P}; ±0.01) of each Q^{n}_{P} contribution extracted by NMR spectra deconvolution.

[b]Peak maximum (δ^{Si}_{max}; uncertainty ±0.15 ppm), the center-of-gravity shift (δ^{Si}_{CG}; ±0.25 ppm), and fwhm height (W_{Si}; ±0.25 ppm) of the net ^{29}Si NMR signal.

Table 3: ^{11}B NMR Results[a]

	$B^{[3]}$			$B^{[4]}$			Populations[b]		BO_3 populations[c]	
label	δ_{CG} (ppm)	$\overline{\delta}_{iso}$ (ppm)	$\overline{C}_{Q\eta}$ (MHz)	δ_{CG} (ppm)	$\overline{\delta}_{iso}$ (ppm)	$\overline{C}_{Q\eta}$ (MHz)	$x_B^{[3]}$	$x_B^{[4]}$	$x_B^{[3]}$(0Si)	$x_B^{[3]}$(1Si)
$S46_{2.6}(5)$	14.00			−0.04	0.12	0.39	0.831	0.169		
$S46_{2.6}(9)$	13.98	18.6	2.72	0.31	0.43	0.35	0.740	0.260	0.76	0.24
$S46_{2.6}(14)$	13.98			0.49	0.59	0.36	0.705	0.295		
$S46_{2.6}(18)$	13.96	18.7	2.74	0.58	0.72	0.35	0.684	0.316	0.86	0.14
$S46_{2.6}(28)$	14.01			0.83	0.94	0.38	0.665	0.335		
$S46_{2.6}(37)$	14.02	18.8	2.70	1.02	1.12	0.39	0.660	0.340	1.00	0.00
$S49_{4.0}(2)$	13.21			−0.47	−0.31	0.37	0.635	0.365		
$S49_{4.0}(5)$	13.22			−0.29	−0.19	0.35	0.612	0.388		
$S49_{4.0}(7)$	13.29			−0.15	−0.01	0.36	0.589	0.411		
$S49_{4.0}(10)$	13.40	18.2	2.70	0.09	0.20	0.37	0.576	0.424	0.70	0.30
$S49_{4.0}(15)$	13.62			0.39	0.49	0.37	0.568	0.432		
$S49_{4.0}(19)$	13.65			0.51	0.61	0.38	0.567	0.433		
$S49_{4.0}(24)$	13.72	18.4	2.72	0.59	0.72	0.40	0.567	0.433	0.83	0.17

[a] $\delta_{CG}(B^{[3]})$ and $\delta_{CG}(B^{[4]})$ with uncertainties of ±0.08 ppm and ±0.04 ppm, respectively, correspond to the center-of-gravity shifts in the MAS NMR spectra. All other NMR parameters for the $^{11}BO_3$ and $^{11}BO_4$ groups were obtained from 3QMAS and MAS ^{11}B NMR spectra, respectively, with uncertainties as follows: $\overline{\delta}_{iso}(B^{[3]})$±0.20 ppm; $\overline{\delta}_{iso}(B^{[4]})$±0.06 ppm; $\overline{C}_{Q\eta}(B^{[3]})$±0.10 MHz; $\overline{C}_{Q\eta}(B^{[4]})$±0.10 MHz.

[b] The fractional populations (uncertainty ±0.01) were obtained by integrating the MAS NMR intensities and then correcting for the satellite-transition contributions to the CT centerband peak.[68]

[c] Relative populations of BO_3 groups without $[x_B^{[3]}(0Si)]$ and with one $[x_B^{[3]}(1Si)]$ bond to Si (uncertainty ±0.03); they are normalized according to $x_B^{[3]}(0Si)+x_B^{[3]}(1Si)=1$.

Figure Captions

Fig. 1. Experimental ^{31}P MAS NMR spectra recorded at 9.4 T from the as-indicated S$N_p(q)$ glasses, with members from the S46 and S49 series shown in the left and right panels, respectively, and listed according to increasing B_2O_3 content from top to bottom. The ^{31}P resonances from the $Q^0_{\rm P}$ (main peak) and $Q^1_{\rm P}$ (minor) groups are indicated, with the fractional populations of the latter specified in %. The curve beneath each NMR spectrum represents the difference between experimental and best-fit data.

Fig. 2. Experimental ^{29}Si MAS NMR spectra obtained at 9.4 T (black traces) from the (a) $S46_{2.6}(0)$ and (b) $S49_{4.0}(0)$ glasses, shown together with the set of $\{Q^n_{\rm Si}\}$ component peaks (gray traces) obtained by spectra deconvolution. Each gray number within (or on top) of each NMR peak specifies its relative population in %. The curve beneath each NMR spectrum represents the difference between the experiment and the corresponding best-fit. (c, d) NMR spectra obtained from glasses with as-specified molar fractions of B_2O_3 from each (c) S46 and (d) S49 series. Note that the results for $S46_{2.6}(0)$—*i.e.*, the "45S5 Bioglass"[15]—are reproduced from Mathew *et al.*[33]

Fig. 3. ^{11}B MAS NMR spectra obtained at 14.1 T from the (a) S46 and (b) S49 glasses for the as-indicated $x(B_2O_3)$ values. The total integrated signal intensity of each NMR spectrum is normalized to unity.

Fig. 4. The fractional population of $B^{[4]}$ groups (out of the total B speciation) plotted against the molar fraction of B_2O_3 for the S46 (solid squares) and S49 (solid circles) glass series. Open symbols represent predictions from the Yun-Dell-Bray-Xiao (YDBX) model.[38]

Fig. 5. (a) 3QMAS ^{11}B NMR spectrum recorded at 14.1 T from the $S46_{2.6}(9)$ glass. (b, c) Zooms around the $^{11}B^{[3]}$ signal region of 3QMAS NMR spectra obtained from (b) $S46_{2.6}(9)$ (black contours); $S46_{2.6}(37)$ (red contours), and (c) $S49_{4.0}(10)$ (black contours); $S49_{4.0}(24)$ (red contours). The arrows mark the directions of the resonance spreads stemming from distributions of isotropic

chemical shifts (marked by "CS") and quadrupolar coupling constants (labeled "Q").

Fig. 6. Projections along the isotropic dimension of 3QMAS ^{11}B NMR spectra (left panel) and MAS spectra (right panel) from the as-indicated S46 and S49 glasses. The black and red traces represent experimental and best-fit peakshapes, respectively: they comprise two signal components at ≈80–82 ppm (gray lines; $^{11}B^{[3]}$(0Si) groups in boroxol rings) and ≈74 ppm (solid areas; $^{11}B^{[3]}$(1Si) moieties). Gray numbers specify the fractional populations (in %) of the $B^{[3]}$(1Si) groups. (k) Ranges of center-of-gravity (CG) shifts along the isotropic projection for $^{11}B^{[3]}$ moieties with 0, 1, 2, and 3 NBO ions, compiled from literature data:[51,55,56,72–79] the white bar marks $\overline{\delta}_{CG}$, whereas the gray and black rectangles depict the total shift-span and $\overline{\delta}_{CG} \pm \sigma$, respectively. (l) As in (k), but illustrating the range of $\{\overline{\delta}_{iso}\}$, which is to be compared with the span of experimentally observed extreme $\overline{\delta}_{iso}$-values (dotted lines) at 18.2 ppm and 18.8 ppm; see Table **3**.

Fig. 7. (a–d) NMR-derived best-fit populations $[x_B^{[4]}(m\text{Si})]$ of BO_4 groups with m B–O–Si bonds observed from the series of (a, b) S46 and (c, d) S49 glasses. The data are plotted against the fractions (a, c, e) $y_B = x_B/(x_B + x_{Si})$ and (b, d, f) $y_B^{[3]} = x_B x_B^{[3]}/(x_B x_B^{[3]} + x_{Si})$. y_B and $y_B^{[3]}$ are relevant for the scenarios of unrestricted $B^{[4]}$–O–$\mathbf{B}^{[3]}$/$\mathbf{B}^{[4]}$/**Si** bond formation and $B^{[4]}$–O–$\mathbf{B}^{[4]}$ avoidance, respectively. (e, f) Average number of Si atoms per BO_4 group ($\overline{N}_{Si}$) obtained from the fractional populations in (a, c) and (b, d), respectively. The experimental data are compared with the as-indicated statistical models, where P_{Si}=0 corresponds to a random bond formation between $B^{[4]}$ and atoms from the set (e) {Si, $B^{[3]}$, $B^{[4]}$} or (f) {Si, $B^{[3]}$}, whereas P_{Si}>0 implies a preference for $B^{[4]}$–O–Si linkages [see eq. (5)]. To improve visualization in (e, f), the error bars (±0.04) are generally suppressed.

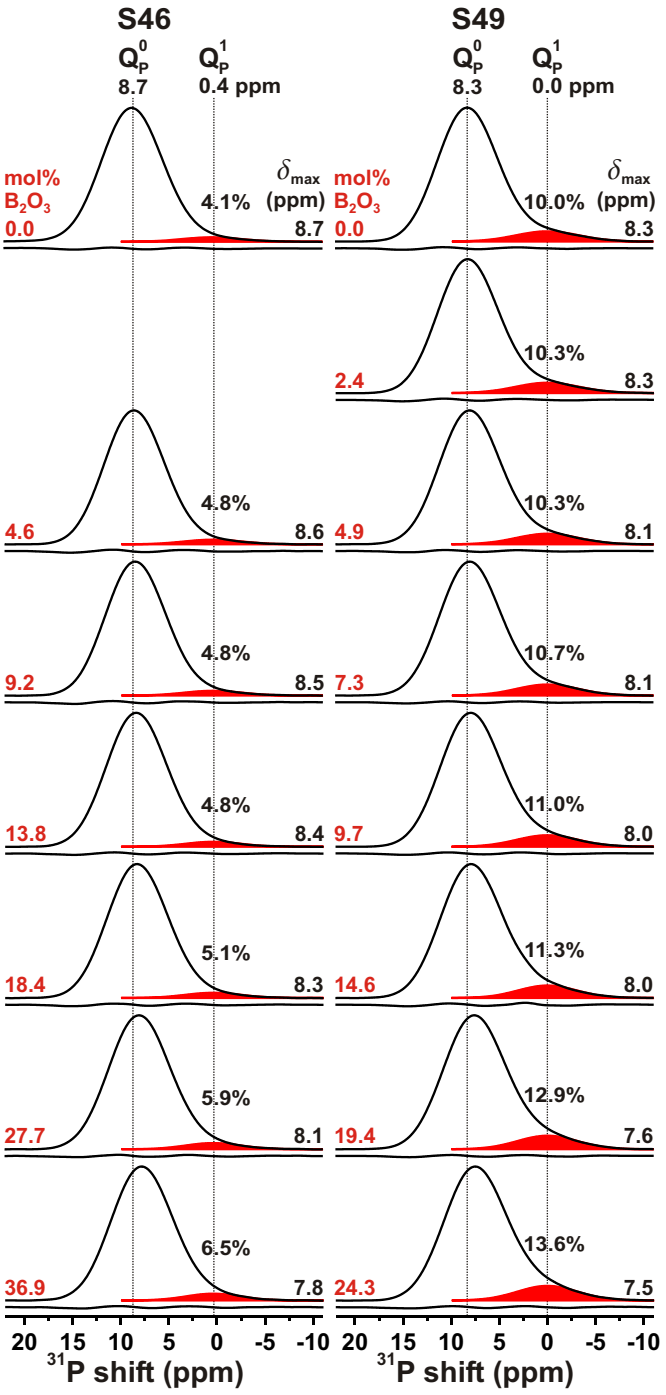

Fig. 1

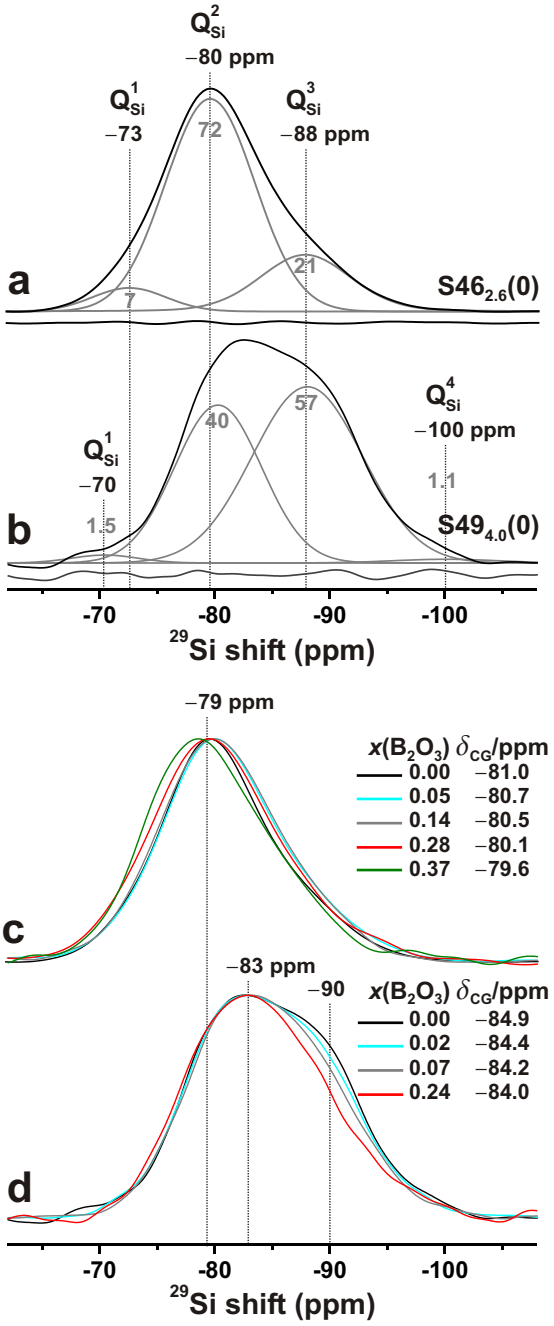

Fig. 2

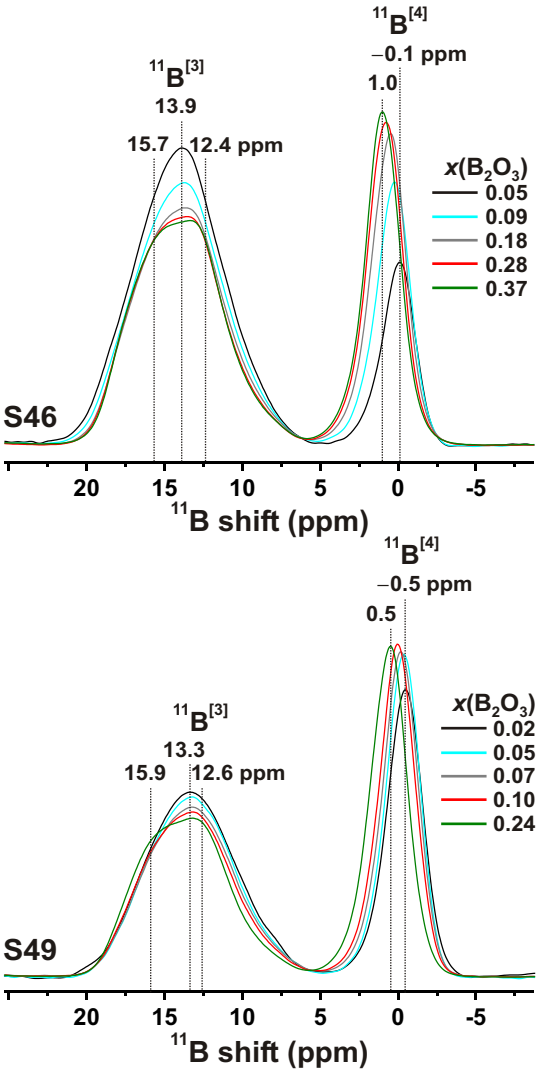

Fig. 3

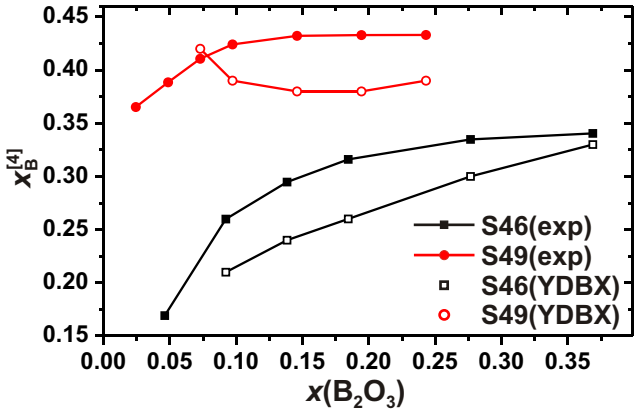

Fig. 4

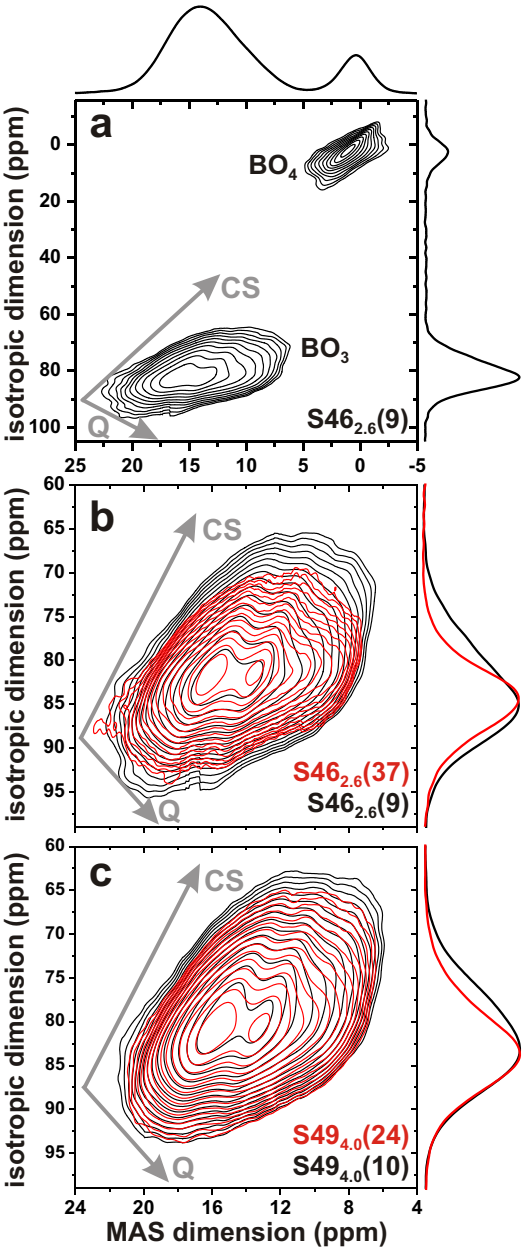

Fig. 5

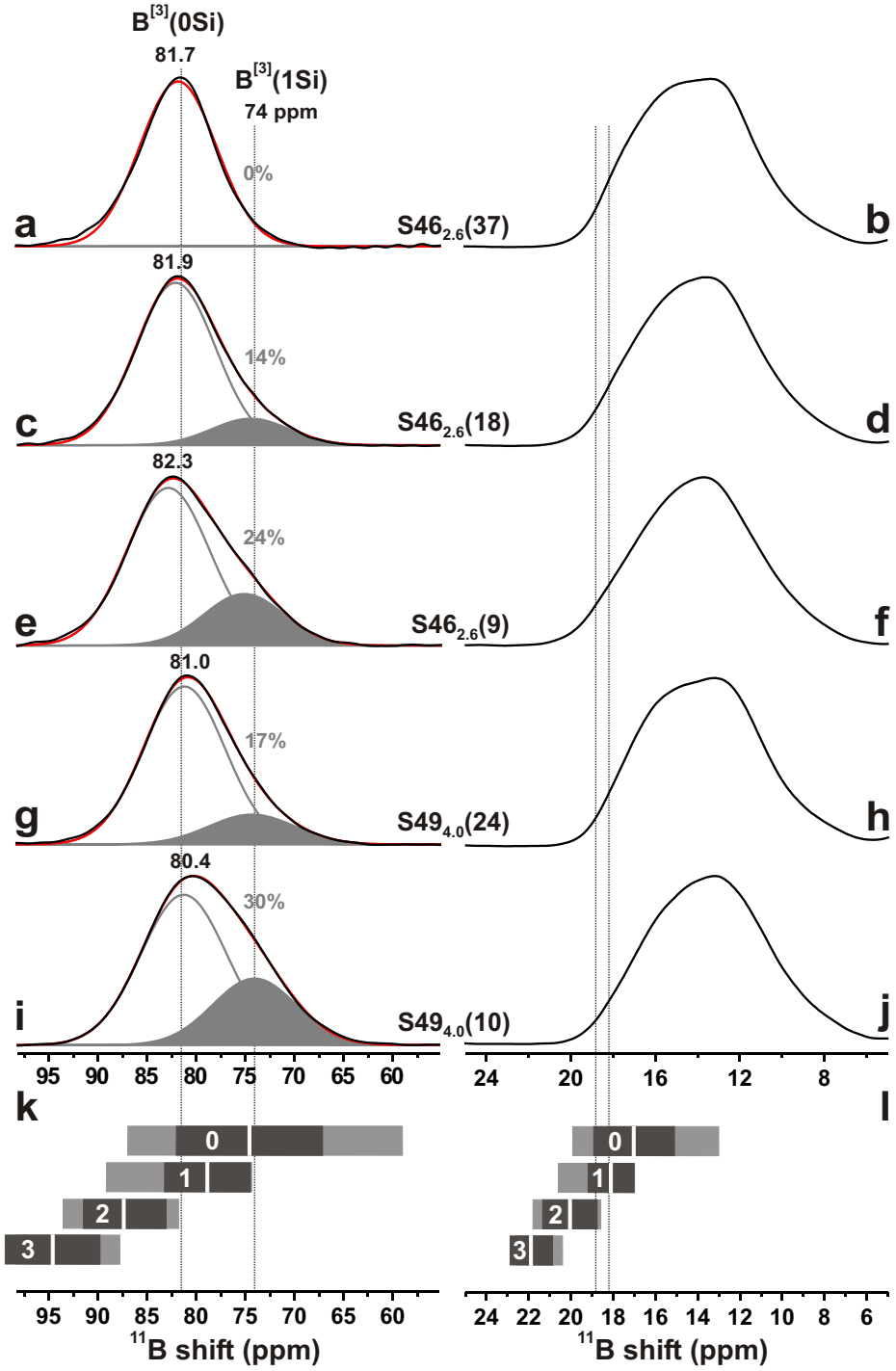

Fig. 6

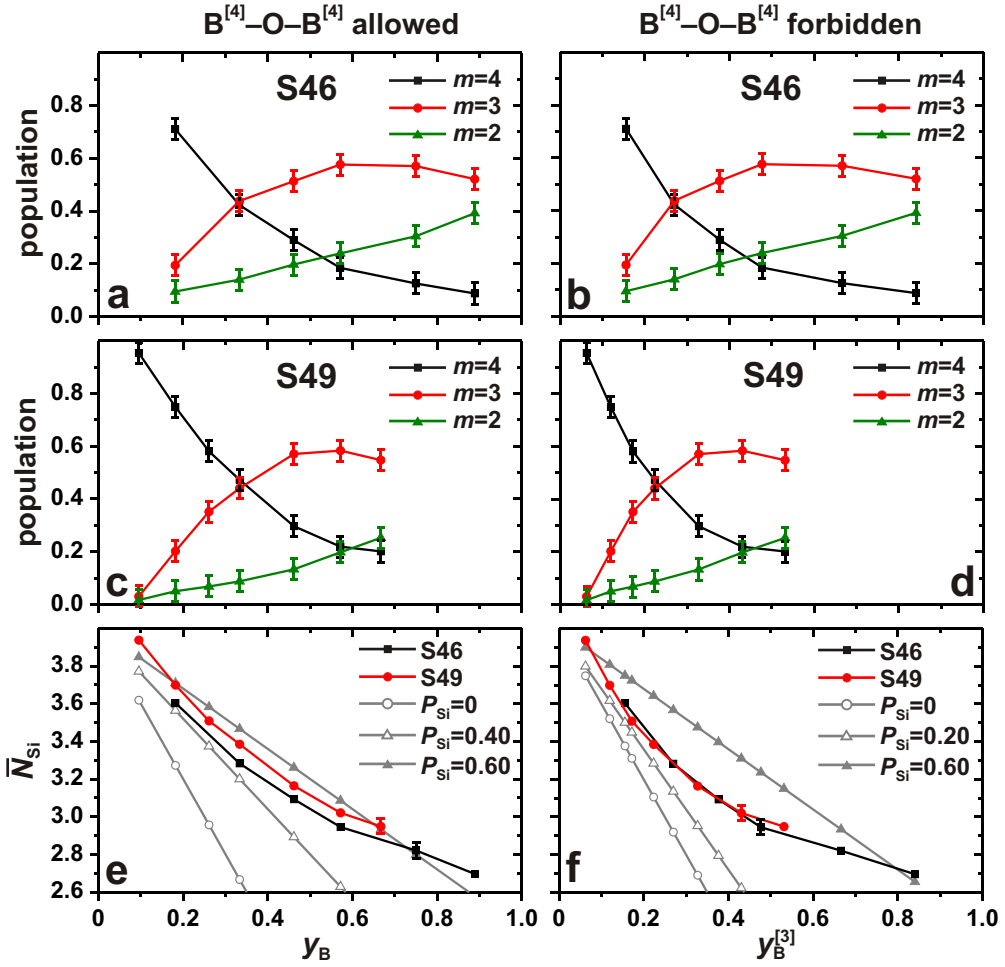

Fig. 7